

UNIVERSITY OF CALIFORNIA, SAN DIEGO

Determination of Oceanic Crustal Shear Velocity Structure
from Seafloor Compliance Measurements

A dissertation submitted in partial satisfaction of the
requirements for the degree of Doctor of Philosophy in Oceanography

by

Wayne Clifford Crawford

Committee in charge:

Research Oceanographer Spahr C. Webb, Co-Chair

Professor John A. Hildebrand, Co-Chair

Professor Henry D.I. Abarbanel

Professor Bruce K. Driver

Professor Robert T. Guza

Professor Robert L. Parker

1994

The dissertation of Wayne Clifford Crawford is approved:

Co-Chair Date

Co-Chair Date

Date

Date

Date

Date

University of California, San Diego

Spring 1994

Contents

Table of Contents	v
List of Figures	vi
List of Figures	vii
Acknowledgments	ix
Vita	xi
Abstract of the Dissertation	xiii
1 Introduction	1
2 Seafloor Compliance	9
2.1 Introduction	9
2.2 Infragravity waves	10
2.3 Seismic surface waves	16
2.4 Appendix: Compliance of a Half-Space	25
3 Seafloor Compliance Observed by Long-Period Pressure and Dis-	
placement Measurements	27
3.1 Introduction	27
3.2 Theory	28
3.3 Inversion	31
3.4 Instrumentation	33
3.5 Measurements	34
3.6 Conclusions	35
3.7 References	36

4	Crustal Aging at the East Pacific Rise, 9°50'N	39
4.1	Introduction	39
4.2	Measurements	43
4.3	Analysis	44
4.4	Inversion	48
4.5	Conclusions	51
5	An Autonomous, Deep-Ocean, Compliance Sensor	53
5.1	Introduction	53
5.2	ADOCS overview	56
5.3	ADOCS hardware	63
5.4	ADOCS software	64
5.5	ADOCS mechanicals	70
5.5.1	Noise sources	70
5.5.2	Calibration	73
5.6	Conclusions	75
6	Juan de Fuca Ridge Shear Velocity Profiles	77
6.1	Introduction	77
6.2	Measurement and Data Analysis	79
6.3	Inversion	82
6.3.1	Cleft segment	84
6.3.2	Coaxial segment	93
6.3.3	Endeavour segment	96
6.4	Conclusions	102
	References	104
	Bibliography	105

List of Figures

1.1	Fast spreading ridge model	3
1.2	Listric and normal faults	5
1.3	Seismic layer 2 models	6
2.1	Typical ocean surface wave spectrum model	11
2.2	Typical ocean seafloor pressure spectrum	12
2.3	Comparison of forced and free infragravity wave energy	15
2.4	Compliance of a half-space	21
2.5	Compliance of sediments over a half-space	23
2.6	Compliance of a low shear velocity zone 1500 mbsf	24
3.1	West Cortez basin spectra and coherences	28
3.2	Axial Seamount spectra and coherences	28
3.3	Earth models and resulting compliances	29
3.4	Compliance sensitivity to shear velocity changes	30
3.5	Compliance depth sensitivity	32
3.6	Inversions of model compliances	33
3.7	Effect of data uncertainty on inversion	33
3.8	Axial Seamount and West Cortez Basin compliances	34
3.9	Inversion starting models	35
3.10	Inversion results	35
4.1	Bathymetry of the East Pacific Rise centered at 9°50'N	42
4.2	EPR forward modeled compliances with measured compliances	45
4.3	Crustal models at 9°35'N on the East Pacific Rise	46
4.4	Compliance dependence on V_P/V_S ratio	49
4.5	EPR shear velocity models	50

5.1	Autonomous Deep-Ocean Compliance Sensor (ADOCS) schematic . . .	55
5.2	Lacoste-Romberg gravimeter diagram	57
5.3	ADOCS internal schematic	60
5.4	Schematic drawing of pendulum seismometers	61
5.5	ADOCS control program	65
5.6	ADOCS automatic leveling subroutine	66
5.7	ADOCS automatic measurement subroutine	67
5.8	ADOCS “catastrophe” subroutine	69
5.9	36-hour ADOCS acceleration signal	71
5.10	Acceleration spectra of ADOCS versus a heated gravimeter	72
6.1	Bathymetry of the Juan de Fuca Ridge	78
6.2	Spectra and coherence at site COAXIAL1	80
6.3	Seafloor compliances measured on the Juan de Fuca Ridge	83
6.4	Shear velocity models determined by inversion of compliances	85
6.5	Compressional velocity models used for compliance inversion	86
6.6	Thick magma chamber models and resulting compliances	88
6.7	Thin magma chamber models and resulting compliances	89
6.8	Compliance depth-frequency relationship	90
6.9	Magma lens over crystal mush models and resulting compliances	91
6.10	Bathymetry of south Coaxial segment, Juan de Fuca Ridge	94
6.11	Deviation of instrument from horizontal level	95
6.12	Site ENDEAV1 layer 2A models and compliances	98
6.13	Starting models and resulting ENDEAV1 V_S inversions	99
6.14	ENDEAV1 inversions using assumed V_P/V_S	100

Acknowledgments

I would like to express my deepest appreciation to my advisors, Spahr Webb and John Hildebrand, who were always available to answer my questions and to suggest new research possibilities. Sea cruises with John were made more enjoyable by his organization, enthusiasm, and seemingly boundless energy. Spahr was patient and thorough in helping me to understand concepts that seemed beyond my grasp, and he was forgiving of the experiments I accidentally sabotaged.

I thank Jacques Lemire and Tom Deaton for assistance in designing the autonomous compliance sensor. Without Tom's electronic design expertise, the instrument would never have worked, and without Jacques' mechanical designs and craftsmanship, the instrument would have fallen apart on the first deployment. I was aided in deployment and recovery of the autonomous compliance sensor by numerous shipboard crewmembers, technicians, engineers, and scientists. In particular, I thank John Boaz, Norm Waters, Tony Boegeman, and Perry Crampton.

I thank my friends — including Steve Mills, Chris Weaver, Sam Labrie, Mike Makanic, Seabury McGown, and John Penvenne — for camping with me, playing frisbee with me, and for thousands of unmentioned but not forgotten acts of kindness. I especially thank Seabury for assisting my research and writing at home and at sea, and for a wonderful bicycle trip across the U.S., and Steve for feigning interest in my thesis topic. Figure 5.1 was beautifully drawn by Jo Griffith, who provided me with wonderful drawings and friendship during my stay in Sverdrup Hall. Finally, I thank my parents for 27 years of support and encouragement.

The text of Chapter Three, in full, is a reprint of the material as it appears in the Journal of Geophysical Research. I was the primary researcher and author and the co-authors listed in that publication directed and supervised the research which forms the basis for the chapter.

Vita

1966	Born September 17, Monterey, California
1988	B. S., Electrical Engineering and Computer Sciences University of California, Berkeley
1988-1994	Research Assistant, Scripps Institution of Oceanography University of California, San Diego
1994	Doctor of Philosophy in Oceanography University of California, San Diego

Publications

Webb, S.C., X. Zhang and W.C. Crawford, Infragravity waves in the deep ocean, *Journ. Geophys. Res.*, **96** (1), 2723–2736, 1991.

Crawford, W.C., S.C. Webb and J.A. Hildebrand, Seafloor compliance observed by long-period pressure and displacement measurements, *Journ. Geophys. Res.*, **96** (9), 16151–16160, 1991.

Fields of Study

Major field: Applied Ocean Sciences

Studies in Physical Oceanography:

Professors Robert T. Guza, Myrl Hendershott, Joseph L. Reid

Studies in Fluid Mechanics:

Professor Clinton D. Winant

Studies in Applied Mathematics:

Professor Bruce Driver

Studies in Geophysics:

Professors Leroy Dorman, Freeman Gilbert, John Hildebrand, Bernard Minster,
Robert L. Parker

Studies in Biological Oceanography:

Professors Walter Heilegenberg, John McGowan, George Sugihara

Studies in Marine Geology and Geochemistry:

Professors Wolf Berger, Jores Gieskes

Studies in Geophysical Data Analysis:

Professor Robert Pinkel

ABSTRACT OF THE DISSERTATION

Determination of Oceanic Crustal Shear Velocity Structure
from Seafloor Compliance Measurements

by

Wayne Clifford Crawford

Doctor of Philosophy in Oceanography

University of California, San Diego, 1994

Research Oceanographer Spahr C. Webb, Co-Chair

Professor John A. Hildebrand, Co-Chair

Compressional wave velocity (V_P), shear wave velocity (V_S), and density are three parameters used to quantify an isotropic elastic solid. Geophysicists have developed methods for determining ocean crustal V_P and have made some progress in constraining crustal densities, but measurements of crustal V_S are often not attainable. This dissertation describes the development of a method to estimate crustal V_S by measuring seafloor motion due to the pressure field exerted by linear ocean surface gravity waves. Seafloor compliance — defined as the transfer function between seafloor acceleration and pressure — depends on crustal structure and is especially sensitive to crustal V_S .

Seafloor pressure and acceleration data are collected with a long-period instrument containing a Lacoste-Romberg gravimeter and a differential pressure gauge. Compliance is calculated from the data and then compliance values are inverted to estimate V_S structure of oceanic crust to depths of approximately 6000 meters below the seafloor (mbsf).

Site compliances are calculated from seafloor data collected at three sites on the East Pacific Rise, five sites on the Juan de Fuca Ridge, and one site in a sedimentary basin in the California Continental Borderlands. V_S profiles of the underlying crust are estimated from compliance data using nonlinear geophysical inverse theory. On the Juan de Fuca Ridge, a V_S profile from Axial Seamount reveals a region of partial melt at a depth of approximately 2500 mbsf. The Cleft segment V_S profile also reveals partial melt starting 2000-2500 mbsf. A site on the Endeavour segment requires a very thick (700 ± 50 m) low velocity layer to match the compliance data. Finally, three measurements across the East Pacific Rise at $9^\circ 50'N$ show a decrease in compliance with age, consistent with layer 2A thinning with age due to alteration of extrusive volcanic rocks.

Chapter 1

Introduction

This thesis discusses the development of a technique — seafloor compliance inversion — to determine oceanic crustal shear velocity structure, and particularly to detect and delimit regions of low shear velocity. The goal of the research is to aid in development and validation of mid-ocean ridge accretion models. Crustal accretion at mid-ocean ridges involves magma transport and eruption, and generates an often highly porous extrusive volcanic layer. Both magma and porous crust have low shear velocities, which can be detected and quantified through measurements of seafloor compliance.

Oceanic crust is produced at mid-ocean ridges by a combination of tectonic extension and magmatic construction. Tectonic extension is caused by gravitational forces that act on the plate at mid-ocean ridges and in subduction zones and possibly by shear traction from mantle convection cells. Magmatic construction arises as hot mantle material upwells beneath the ridges and partially melts due to the decrease

in pressure as the material rises.

The shape, amount of faulting, and magmatic plumbing system of mid-ocean ridges is highly variable. However, several major aspects of ridge morphology and inferred magma supply are correlated to ridge spreading rates. Slow spreading ridges such as the Mid-Atlantic Ridge (full spreading rate 1.8 cm/yr at 33°S) are heavily faulted and have a broad axial valley, while fast spreading ridges such as the East Pacific Rise at 9°N (full spreading rate 11.2 cm/yr) appear to be only lightly faulted, and usually have a maximum height along the ridge axis. These differences in ridge morphology are inferred to reflect differences in magma supply beneath the ridge, with fast-spreading ridges overlying a continuous or nearly continuous melt lens 1000–2000 meters below the seafloor (mbsf), while slow-spreading ridge magma chambers are deeper and discontinuous along-axis. All mid-ocean ridges may be offset by axial discontinuities ranging from barely distinguishable *devals* (deviations in axial linearity) to several hundred kilometer long transform faults.

Fast-spreading ridges studied to date have a magmatic supply robust enough to fill in the gaps created by tectonic extension. Therefore, the ridges are relatively unfaulted and oceanic crustal structure is consistent along and across the ridge. *Ophiolites* (large sections of oceanic crust that have been uplifted above sea level at convergent plate boundaries) reveal the oceanic crustal sequence as extrusive lavas over sheeted dikes over gabbros over mantle rocks (figure 1.1). The extrusive lavas include pillow lavas and sheet flows; *Bonatti and Harrison* [1988] assert that the ratio of pillow lavas to sheet flows correlates to the temperature and viscosity of

Figure 1.1: Oceanic crustal model of a fast spreading ridge (from *Kent et al.* [1993]).

the magma, which is a function of magmatic supply to the ridge. Relatively hot, low viscosity magma associated with robust magmatic supply will result in a high percentage of sheet flows, whereas relatively cool, high viscosity magmas encounter higher thermal stresses during extrusion, which result in predominant pillow lava formation. Fresh pillow lavas have significantly lower shear velocity than sheet flows because of the open spaces between the pillows. As these spaces are filled in by hydrothermal alteration of the pillows, the shear velocity of the extrusive layer decreases. Below the extrusive layer, the sheeted dikes record the passage of magma from the melt lens to the surface. Below the sheeted dikes, the gabbroic layer is generated from the cooling outer edges of the melt lens and underlying crystal mush as the plates move away from the spreading center.

Where magmatic construction cannot keep up with tectonic extension (usually on slow-spreading ridges), mid-ocean ridges are heavily faulted, particularly by low-range normal or listric faulting (figure 1.2). Extensive faulting is created by the imbalance of tectonic extension over volcanic construction. The extensional stress-induced faulting thins the crust and exposes *plutonic* (non-extrusive volcanic) rocks at the seafloor. Additional stress is generated when the newly exposed plutonic rocks are hydrated, resulting in a decrease in rock density. Magma is discontinuous along the ridge and emplaced deeper than on fast spreading ridges. The extrusive volcanic layer varies in thickness along and across axis, suggesting that magmatic supply is episodic. Slow-spreading ridge axes often lie within a broad axial valley with steep walls constructed by faulting.

Figure 1.2: Models of deep listric faults found on slow spreading ridges (from *Salisbury and Keen* [1993]).

Medium-spreading ridges, such as the Juan de Fuca Ridge in the northeast Pacific ocean (full spreading rate 6 cm/yr), have morphologies and inferred magma supplies that fall between the extremes of fast and slow spreading ridges. The Juan de Fuca Ridge is more highly segmented than the fast-spreading East Pacific Rise, and magma supply is probably discontinuous across segments, but there is no evidence of plutonic rocks at the surface, and axial valleys are much smaller than on the slow-spreading Mid-Atlantic Ridge.

One of the most successful methods of determining mid-ocean ridge structure is to estimate crustal compressional velocities using active seismic profiling. Petrologic structure is inferred from mid-ocean ridge models constructed through direct study of oceanic crustal rocks at deep ocean drilling holes and in ophiolites.

Figure 1.3: Models of the petrologic structure associated with seismic layer 2 at the East Pacific Rise (from *Harding et al.* [1993]).

Because the seismic velocity structure does not directly correlate with petrologic structure, seismologists describe seismic models as layers numbered 1–4. Layer 1 is the sediments. Layer 2, a region of rapid seismic velocity increase with depth, is the top oceanic crustal layer. Below layer 2 lies layer 3, a higher velocity layer with very little change in seismic velocity. Finally, there is a jump in velocity to layer 4, another nearly constant velocity layer. Layer 2 is inferred to correspond to the extrusive volcanics and sheeted dikes, layer 3 the gabbros, and layer 4 mantle rocks and the mantle/gabbro interface. Layer 2 is further divided into layers 2A (the region of highest velocity gradient, usually associated with young, unaltered extrusives), 2B (altered extrusives and the interface between extrusives and dikes), and 2C (sheeted dikes). Figure 1.3 shows examples of the relationship between seismic layer 2 and petrologic layers.

We use seafloor compliance to estimate oceanic crustal shear velocities. Shear velocities are especially sensitive to rock porosity (found in the extrusive vol-

canic layer) and to partial melt (found in melt lenses and underlying crystal mush). Determination of crustal shear velocity structure allows analysis of the existence, location, and across- and along-strike variability of magma chambers; the change in layer 2A thickness with age; and the ratio of pillow lavas to sheet flows in the extrusive volcanic layer. This dissertation includes shear velocity determinations from compliance measurements at a fast-spreading center (the East Pacific Rise) and a medium-rate spreading center (the Juan de Fuca Ridge).

Chapter 2 describes the physical processes that allow compliance measurement. Analytic calculations of compliance of very simple earth models are presented and their relevance to compliance of oceanic crust is discussed.

Chapter 3 presents compliance data collected using a tethered gravimeter from two structurally distinct seafloor sites: 1) a sediment-filled basin and 2) the intersection of a hotspot chain and a mid-ocean ridge. Seafloor compliance differences between the two sites are caused by the different physical properties of the seafloor at the two sites. Inversion of seafloor compliance for oceanic crustal structure is introduced and explained. Inversion at the mid-ocean ridge site (the caldera of an active seamount on the Juan de Fuca Ridge) reveals a region of partial melt beneath the edifice.

Chapter 4 describes an experiment to investigate young oceanic crustal aging using a tethered Lacoste-Romberg gravimeter. Compliance was measured at three sites across the East Pacific Rise at crustal ages of 0, 0.18, and 0.4 million years. The compliances show a significant change in crustal structure with age,

corresponding to thinning of seismic layer 2A due to hydrothermal alteration of the extrusive volcanic layer.

Chapter 5 describes the autonomous compliance sensor, developed to improve the quality of compliance measurements while decreasing ship time demands. The compliance data in chapters 3 and 4 were collected by a gravimeter lowered from a research vessel on a deep-ocean cable that supplies power and communication to the instrument. The tethered instrument can be deployed from a ship for a maximum of four hours at one site, while the autonomous instrument allows deployments for as long as battery power is available (> 30 days).

Chapter 6 discusses seafloor compliance measured at four sites on the Juan de Fuca Ridge using the autonomous compliance sensor. Compliance uncertainties for these data are significantly less than for compliances estimated from data collected using the tethered gravimeter. Compliance inversion reveals a region of low shear velocity beneath the Cleft segment, probably corresponding to a melt lens with an upper bound 2000-2500 meters below the seafloor (mbsf). Compliance data from a site on the Endeavour segment can be fit only by a shear velocity model with a thick (700 ± 100 m) layer 2A, indicating the extrusive layer is composed mainly of pillow lavas rather than sheet flows. Compliance data from the CoAxial segment show no evidence of partial melt at depth, despite a recent (60 days before) swarm of microearthquakes in the area interpreted as upwelling and lateral injection of magma either along the ridge axis or within the north rift zone of Axial volcano, a large on-axis seamount.

Chapter 2

Seafloor Compliance

2.1 Introduction

Seafloor compliance $\xi(\omega)$ is defined as the transfer function between vertical displacement u_z and stress τ_{zz} at the seafloor:

$$\xi(\omega) \equiv \frac{u_z}{\tau_{zz}} \Big|_{z=0}. \quad (2.1)$$

Seafloor compliance is measured at periods of 30-300 seconds because the seafloor stress field at those periods is caused by waves with a simple frequency-wavenumber relationship. Compliance is a function of oceanic crustal elastic parameters, and is especially sensitive to shear velocity variations.

This chapter describes the source of seafloor stress fields and explains the dependence of the resulting seafloor motion on oceanic crustal structure. This dissertation uses the following notation for the partial derivatives of displacement:

$$\ddot{u} \equiv \frac{\partial^2 u}{\partial t^2} \quad (2.2)$$

$$u_{,x} \equiv \frac{\partial u}{\partial x}$$

$$u_{i,l} \equiv \sum_{i=1}^3 u_{i,i}.$$

2.2 Infragravity waves

Deep-ocean seafloor compliance is studied in the frequency range 0.002–0.03 Hz (the infragravity wave band) because the seafloor stress field has a simple frequency-wavenumber relation. To calculate seafloor motion under a stress field, the wavenumbers of the stress field must be calculable from easily determined parameters, such as wave frequency and water depth. Infragravity waves measurable on the deep seafloor are linear surface gravity waves described by the equation:

$$\zeta(\mathbf{x}, t) = a \cos(\mathbf{k} \cdot \mathbf{x} - \omega t) \quad (2.3)$$

and the dispersion relation

$$\omega^2 = gk \tanh(kH), \quad (2.4)$$

where a is the wave amplitude, \mathbf{k} the wavenumber, ω the angular frequency, H the water depth, and g is the local gravitational acceleration. We refer to linear ocean surface gravity waves as *free* waves, to distinguish them from the *forced* wave energy that can be generated through nonlinear wave-wave interactions.

At the sea surface, infragravity wave energy is negligible. Figure 2.1 shows a simple model for a wind-driven ocean surface wave power spectrum, which is dominated by free waves and decays exponentially below 0.1 Hz. The spectrum ignores

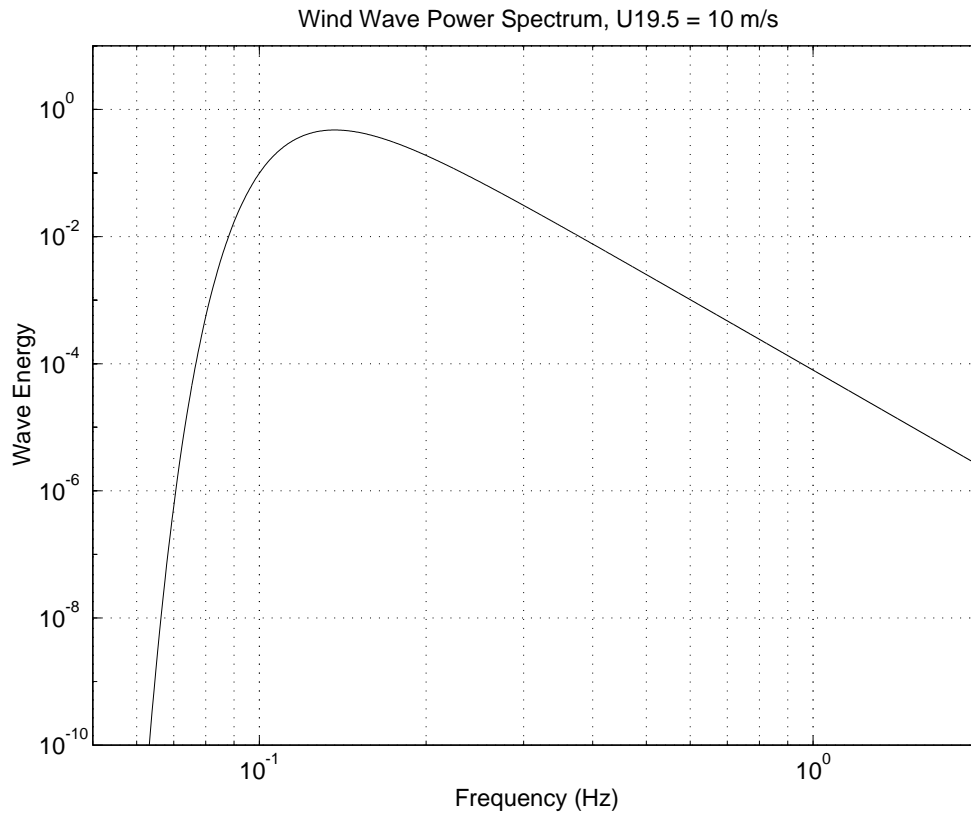


Figure 2.1: Typical ocean surface wave spectrum model

the swell component from distant waves and assumes fully-developed wind-driven waves with a wind velocity of 10 m/s, 19.5 m above the mean sea surface.

The linear wind waves which dominate the surface spectrum contribute negligible energy to the deep ($> 1000 \text{ m}$) seafloor because they have wavelengths much shorter than the ocean depth, and energy decays with depth from the surface as $\cosh(kH)$. Instead, significant energy is found in the infragravity wave band

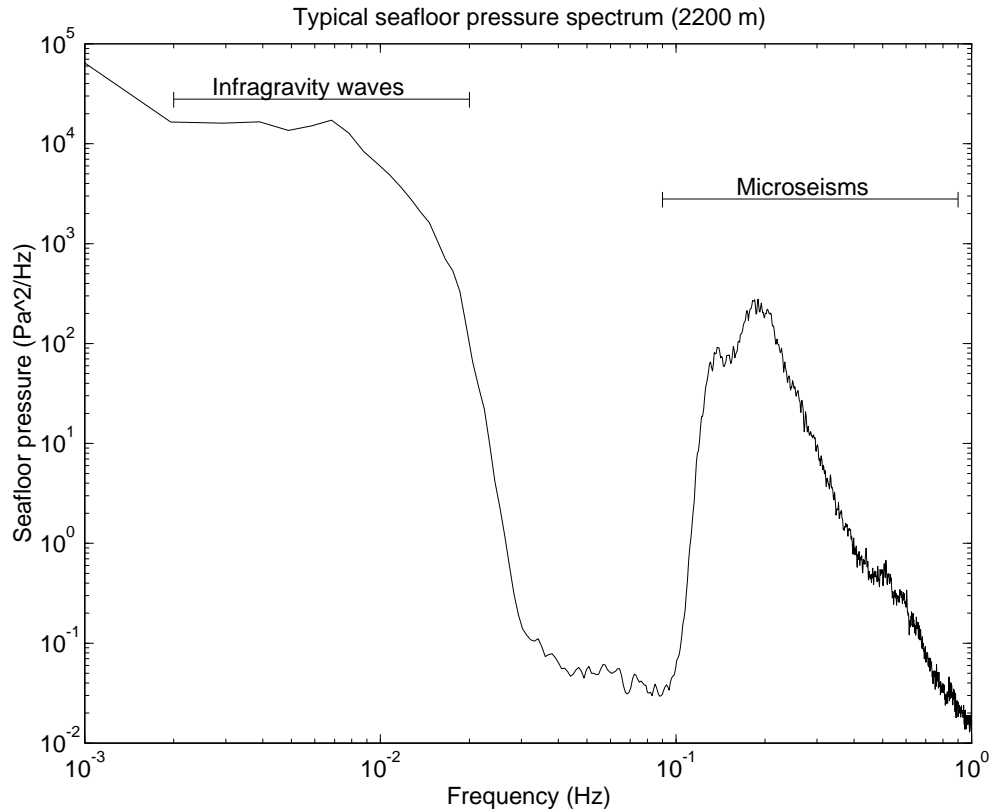


Figure 2.2: Typical ocean seafloor pressure spectrum

(approximately 0.001 Hz to 0.04 Hz) and the microseism band (approximately 0.1 Hz to 2 Hz) (figure 2.2). Waves in these frequency bands are much smaller at the sea surface than linear wind waves, but they have wavelengths longer than the ocean depth, and so their pressure signal hardly decays between the sea surface and the seafloor. Microseisms are nonlinear waves with long wavelengths caused by the subtraction of wavenumbers of two interacting surface waves. Infragravity waves measured on the deep seafloor are linear surface gravity waves generated by

nonlinear interactions at ocean boundaries. The apparent infragravity wave low frequency limit in figure 2.2 is either caused by low frequency instrument noise or by the intrusion of nonlinear waves in the infragravity band, and the upper frequency limit depends on the ocean depth. The microseism energy bandwidth depends on the sea surface energy bandwidth (figure 2.1). Microseisms are forced waves, making their wavenumber-frequency relation difficult to determine and rendering microseism energy useless for compliance inversion.

The infragravity wave band actually contains both forced and free waves. Infragravity wave energy is created as forced waves generated by non-linear wave-wave interactions resulting in products of the sinusoidal terms in equation 2.3 when two free waves interact, which can be expressed as sums and differences of the wave frequencies and wavenumbers. Two waves with wavenumbers and frequencies (ω_1, \mathbf{k}_1) and (ω_2, \mathbf{k}_2) force second-order wave motions with wavenumbers and frequencies $(\omega_1 \pm \omega_2, \mathbf{k}_1 \pm \mathbf{k}_2)$. The forced motion does not fall on the surface gravity dispersion curve, so the forced waves remain much smaller than the forcing waves. Like microseisms, forced infragravity wavenumbers are not directly related to frequency by a dispersion relation; they are also a function of forcing wave frequencies and directions.

Most free infragravity wave energy is generated at ocean boundaries, where local forced infragravity waves are converted into free infragravity waves by nonlinear processes associated with shoaling. Most free infragravity wave energy is refractively trapped in shallow coastal waters, but some leaks out into the deep ocean where the

waves can travel across the ocean with almost no attenuation.

Calculations of seafloor compliance require both frequency and wavenumber values. Because forced infragravity wavenumbers cannot be determined from the frequency and water depth, they only contribute noise to compliance measurements. Fortunately, forced infragravity waves have shorter wavelengths than free infragravity waves, and do not usually contribute significant energy to the seafloor. In the worst case, all forcing waves travel in the the same direction (the spectrum is *colinear*), so that the forcing wavenumbers directly subtract from one another. The forcing waves have wavelengths much shorter than the ocean depth ($kH \gg 1$), so equation 2.4 simplifies to $\omega_n^2 = gk_n$, and the dispersion relation for the forced wave is

$$k_{forced} = k_1 - k_2 = \frac{\omega_1^2 - \omega_2^2}{g} = \frac{\omega_{forced}(\omega_1 + \omega_2)}{g}. \quad (2.5)$$

The seafloor forced infragravity wave energy spectrum $E_{forced,deep}(\omega)$ is calculated from the sea surface forced infragravity wave energy spectrum $E_{forced,surf}(k, \omega)$:

$$E_{forced,deep}(\omega) = \int \frac{E_{forced,surf}(k, \omega)}{\cosh^2(kH)} dk \quad (2.6)$$

Figure 2.3 compares the seafloor free infragravity wave pressure spectrum to a forced infragravity wave spectrum modeled from the surface wave spectrum of figure 2.1 using the colinear assumption. Only the lowest frequency forced infragravity waves (in this case, frequencies ≤ 0.003 Hz) have wavelengths long enough to contribute a significant amount of energy to the seafloor. When wind speeds increase above 10 m/s, the surface wave spectrum peak shifts to lower frequency, allowing forced infragravity waves to contribute energy to the seafloor at higher frequencies. In

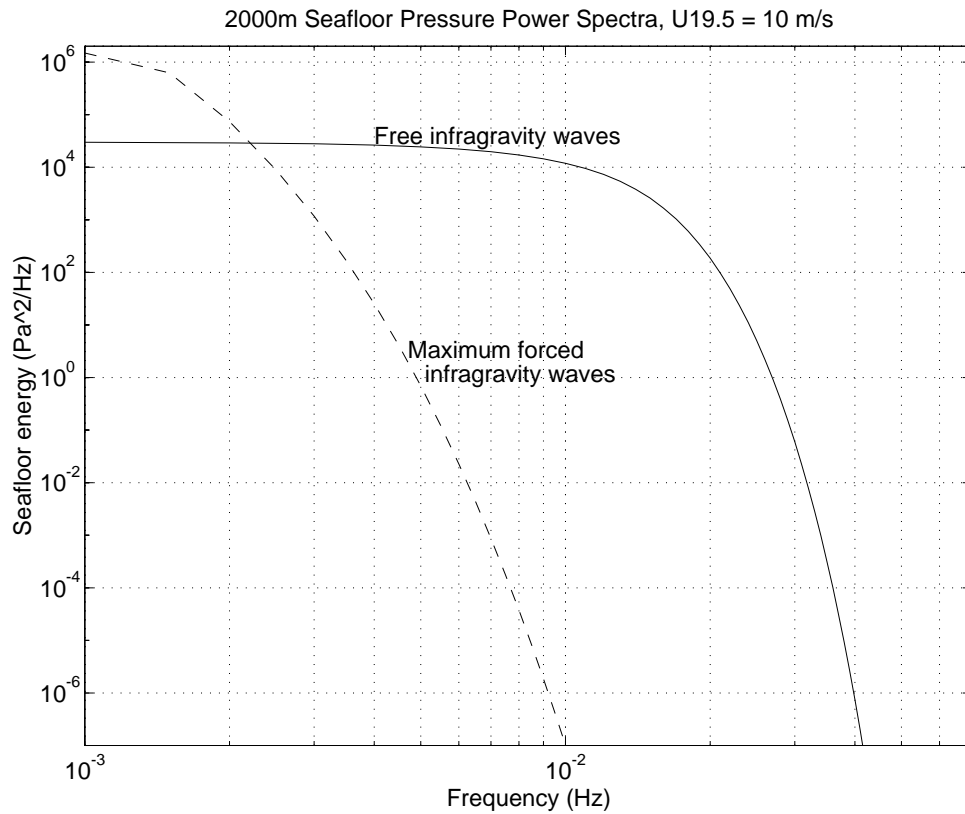


Figure 2.3: Modeled seafloor pressure signal of free infragravity waves (solid line) and forced infragravity waves (dashed line), assuming a 2000 m deep ocean. Forced wave energy is derived from the surface spectrum of figure 2.1, assuming ocean surface wind waves are colinear. The colinear assumption generates the longest wavelength forced waves, resulting in the greatest possible forced wave seafloor pressure signal. Free wave energy is independent of the local surface wave spectrum.

general, wind speeds average less than 10 m/s and the forcing waves do not all travel in the same direction, so forced waves should not contribute a significant amount of energy to the deep seafloor in the compliance frequency band. This is confirmed by pressure measurements on the deep seafloor at frequencies between 0.003 and 0.03 Hz that are dominated by free infragravity waves [Webb *et al.*, 1991].

2.3 Seismic surface waves

The deep seafloor moves underneath infragravity waves with an amplitude that depends on crustal structure. Using a one-dimensional earth model, and assuming the seafloor materials are linearly elastic and isotropic, the stress-strain relationship for a material is

$$\tau_{ij} = \lambda u_{l,l} \delta_{ij} + 2\mu e_{ij}, \quad (2.7)$$

where τ_{ij} is the i component of stress acting on a surface whose normal points in the x_j direction, and $e_{ij} = \frac{1}{2}(u_{i,j} + u_{j,i})$. Assuming wave propagation in the x direction, and a crustal model that varies only in the z direction, results in stresses τ_{zz} and τ_{xz} . Equation 2.7 expands to

$$\tau_{zz} = \lambda u_{l,l} + 2\mu u_{z,z} \quad (2.8)$$

$$\tau_{xz} = \mu (u_{x,z} + u_{z,x}).$$

Using Newton's second law to relate seafloor motion to stress results in

$$\rho \ddot{u}_i = \tau_{ij,j} \quad (2.9)$$

which, combined with the stress-strain relation (equation 2.9) produces the equation of motion for a linearly elastic isotropic material:

$$\rho \ddot{\mathbf{u}} = (\lambda + 2\mu) \nabla (\nabla \cdot \mathbf{u}) - \mu \nabla \times (\nabla \times \mathbf{u}). \quad (2.10)$$

To solve the equation of motion (equation 2.10), we use Helmholtz' theorem, which allows any sufficiently smooth vector field \mathbf{u} to be represented using a vector potential $\mathbf{\Psi}$ and an independent scalar potential φ :

$$\mathbf{u} = \nabla \varphi + \nabla \times \mathbf{\Psi}. \quad (2.11)$$

Substituting equation 2.11 into equation 2.10 results in

$$\rho (\nabla \ddot{\varphi} + \nabla \times \ddot{\mathbf{\Psi}}) = (\lambda + 2\mu) \nabla (\nabla \cdot (\nabla \varphi + \nabla \times \mathbf{\Psi})) - \mu \nabla \times (\nabla \times (\nabla \varphi + \nabla \times \mathbf{\Psi})), \quad (2.12)$$

which is simplified using the vector identities $\nabla \cdot (\nabla \times \mathbf{a}) = 0$, $\nabla \times (\nabla \mathbf{a}) = 0$, and $\nabla^2 \mathbf{a} = \nabla (\nabla \cdot \mathbf{a}) - \nabla \times (\nabla \times \mathbf{a})$ to:

$$\rho (\nabla \ddot{\varphi} + \nabla \times \ddot{\mathbf{\Psi}}) = (\lambda + 2\mu) \nabla (\nabla \cdot \nabla \varphi) + \mu \nabla^2 (\nabla \times \mathbf{\Psi}). \quad (2.13)$$

The final assumption is that the seafloor is piecewise homogeneous. Under this assumption, the seafloor must be modeled as a finite number of homogeneous layers overlying a homogeneous half-space. This assumption allows the elastic parameters to be moved around inside and outside of the gradient and divergence operators, resulting in

$$\nabla [(\lambda + 2\mu) \nabla^2 \varphi - \rho \ddot{\varphi}] = \nabla \times [\mu \nabla^2 \mathbf{\Psi} - \rho \ddot{\mathbf{\Psi}}]. \quad (2.14)$$

Since φ and Ψ are independent, each term in brackets must be equal to zero, so that:

$$\begin{aligned}\ddot{\varphi} &= [(\lambda + 2\mu)/\rho] \nabla^2 \varphi \\ \ddot{\Psi} &= (\mu/\rho) \nabla^2 \Psi.\end{aligned}\tag{2.15}$$

Because the infragravity waves provide plane-wave forcing, $\varphi = \varphi(z)e^{i(\omega t + kx)}$ and $\Psi = \Psi(z)e^{i(\omega t + kx)}$, leading to

$$\begin{aligned}\varphi_{,zz} &= (k^2 - \omega^2/\alpha^2)\varphi \\ \Psi_{,zz} &= (k^2 - \omega^2/\beta^2)\Psi,\end{aligned}\tag{2.16}$$

where $\alpha^2 = (\lambda + 2\mu)/\rho$ and $\beta^2 = \mu/\rho$. Ψ and φ are seismic compressional (P) and shear (S) waves, with phase velocities $V_P = \alpha$ and $V_S = \beta$. A solution for the plane wave forcing problem is

$$\begin{aligned}\varphi(z) &= a_1 e^{-rz} + a_2 e^{rz} \\ \Psi(z) &= \mathbf{b}_1 e^{-sz} + \mathbf{b}_2 e^{sz},\end{aligned}\tag{2.17}$$

where

$$\begin{aligned}r &= \sqrt{k^2 - \omega^2/V_P^2} \\ s &= \sqrt{k^2 - \omega^2/V_S^2}.\end{aligned}\tag{2.18}$$

If the infragravity wave speed $c \equiv \omega/k$ is less than the seismic velocities V_P and V_S , then r and s are real and the waves are *evanescent* (they exponentially decay or grow with depth). If c is greater than V_P or V_S , then r and s are imaginary and the waves propagate through the layer. For a surface wave, the bottom half-space

must have V_P and V_S greater than c , with the boundary condition that the waves decay exponentially with increasing depth ($a_1 = \mathbf{b}_1 = 0$) in the bottom half-space (otherwise energy would increase exponentially to infinity away from the seafloor). Two other boundary conditions for the problem are $\tau_{xz} = 0$ at the seafloor (the free-slip condition) and $\tau_{zz} = 1$ at the seafloor (compliance is independent of stress). Plane-wave forcing results in only one component of the shear wave potential being excited (the vertical, or SV component), so \mathbf{b}_1 and \mathbf{b}_2 can be replaced with scalars b_1 and b_2 .

The only analytical solution determined for compliance is for a homogeneous (half-space) earth model with $V_P, V_S \gg c$:

$$\xi_{hs} = \frac{-V_P^2}{2V_S^2 k \rho (V_P^2 - V_S^2)} = -\frac{\lambda + 2\mu}{2\mu k (\lambda + \mu)}. \quad (2.19)$$

We use normalized compliance $\xi_{norm}() \equiv -k\xi()$, resulting in positive, constant compliance for a half-space model. The partial differences of normalized compliance are:

$$\begin{aligned} \frac{\partial \xi_{norm}(hs)}{\partial V_P} &= -\frac{V_P}{\rho (V_P^2 - V_S^2)} \\ \frac{\partial \xi_{norm}(hs)}{\partial V_S} &= -\frac{V_P}{V_S} \left(\left(\frac{V_P}{V_S} \right)^2 - 2 \right) \frac{V_P}{\rho (V_P^2 - V_S^2)} \\ \frac{\partial \xi_{norm}(hs)}{\partial \rho} &= -\frac{V_P}{2\rho} \left(\left(\frac{V_P}{V_S} \right)^2 - 1 \right) \frac{V_P}{\rho (V_P^2 - V_S^2)}. \end{aligned} \quad (2.20)$$

All of the partials are negative; normalized compliance decreases when density or seismic velocities increase.

Seafloor compliance is a useful measure of oceanic crustal shear velocities

because it is generally much more sensitive to crustal shear velocities than to compressional velocities or density. For oceanic crust, $1.8 < V_P/V_S < 2.4$, so that

$$2 \frac{\partial \xi_{norm}(hs)}{\partial V_P} < \frac{\partial \xi_{norm}(hs)}{\partial V_S} < 9 \frac{\partial \xi_{norm}(hs)}{\partial V_P}. \quad (2.21)$$

Using equation 6.2 to relate ρ to V_P

$$\frac{\partial \xi_{norm}(hs)}{\partial \rho} < \frac{\partial \xi_{norm}(hs)}{\partial V_S} < 8 \frac{\partial \xi_{norm}(hs)}{\partial \rho}. \quad (2.22)$$

ξ_{V_S} and ξ_{ρ} are approximately equal when $V_P/V_S = 1.8$ (non-fractured rock). In addition to having a greater relative effect on compliance than V_P and ρ , V_S is more variable in ocean crust than V_P , which is much more variable than ρ (assuming a V_P range of 2–8 km/s, equation 6.2 generates $\frac{1}{11} < \frac{\partial \rho}{\partial V_P} < \frac{1}{2}$).

Throughout this dissertation, seafloor compliances are calculated from seafloor models of a series of homogeneous layers overlying a half-space, with stresses and displacements continuous across layer interfaces. We use a computer program [Gomberg and Masters, 1988] that starts with unknown P and S wave amplitudes in the bottom half-space, and propagates the waves up to the surface, where the amplitudes are obtained by forcing the waves to match the surface boundary conditions $\tau_{zx} = 0$ and $\tau_{zz} = 1$. The computer program converts stresses and displacements to six minor vectors in order to obtain stable numerical behavior.

Figure 2.4 shows normalized seafloor compliance as a function of phase speed c and frequency for a uniform half-space under 2000 m of water. The dashed line shows the linear surface gravity wave dispersion curve where seafloor compliance is measured. Normalized compliance is constant versus frequency for $c \ll V_S, V_P$

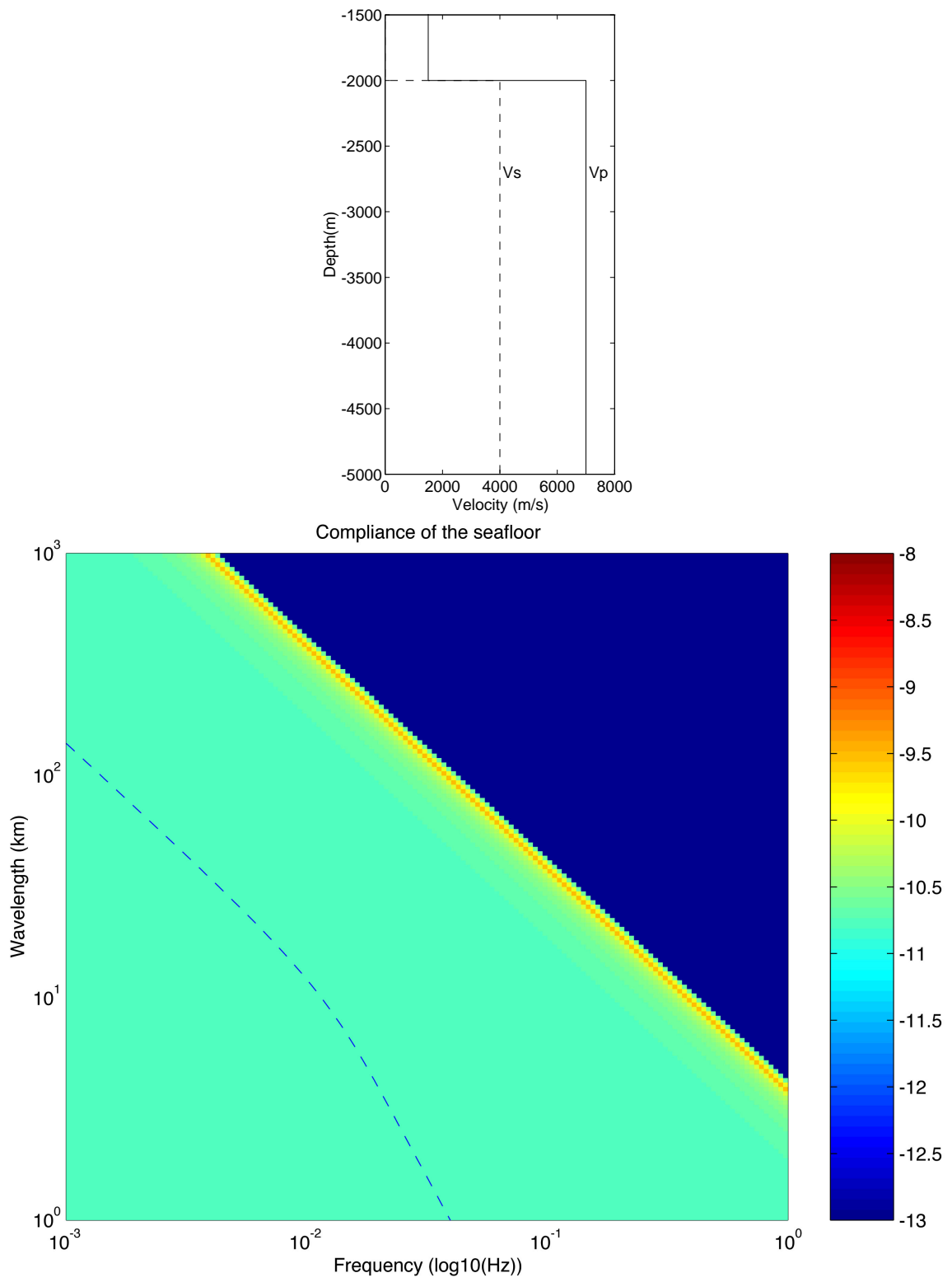


Figure 2.4: Compliance of a half-space

(confirming equation 2.19). As c approaches V_S , the assumptions used to derive equation 2.19 become invalid, and compliance is no longer constant. At $c \approx 0.92V_S$ a nondispersive Rayleigh wave is excited.

Figure 2.5 shows seafloor compliance in a model of a 400 m thick layer of sediments overlying a uniform half-space, all beneath 2000 m of water. The lines of high compliance (actually, infinite compliance) are the poles associated with surface wave normal modes (Stonely waves). There are two dominant Stonely wave phase speeds — one at $c \approx 92\%$ of the hard rock half-space V_S , and another at $c \approx 92\%$ of the sediment layer V_S — which arise for wavelengths shorter than the sediment layer depth. Compliance measured using infragravity waves (dotted line) increases with increasing frequency.

Figure 2.6 shows seafloor compliance in a model of 1500 m of hard rock overlying a 100m-thick low shear velocity layer overlying a hard rock half-space, all beneath 2000 m of water. Measured compliance has a pseudomode (a peak in compliance that crosses modes and follows a continuous frequency-wavenumber function) that arises from the free-slip condition at the top of the half-space. The pseudomode function depends on the thickness and physical properties of the crust overlying the low velocity zone.

Compliance in this dissertation refers to the vertical motion of the seafloor under vertical stress. Horizontal displacements are also excited by the plane wave field; it would be useful to measure “horizontal compliance.” Horizontal compliance measurements would provide better constraints for crustal V_S estimation, and might

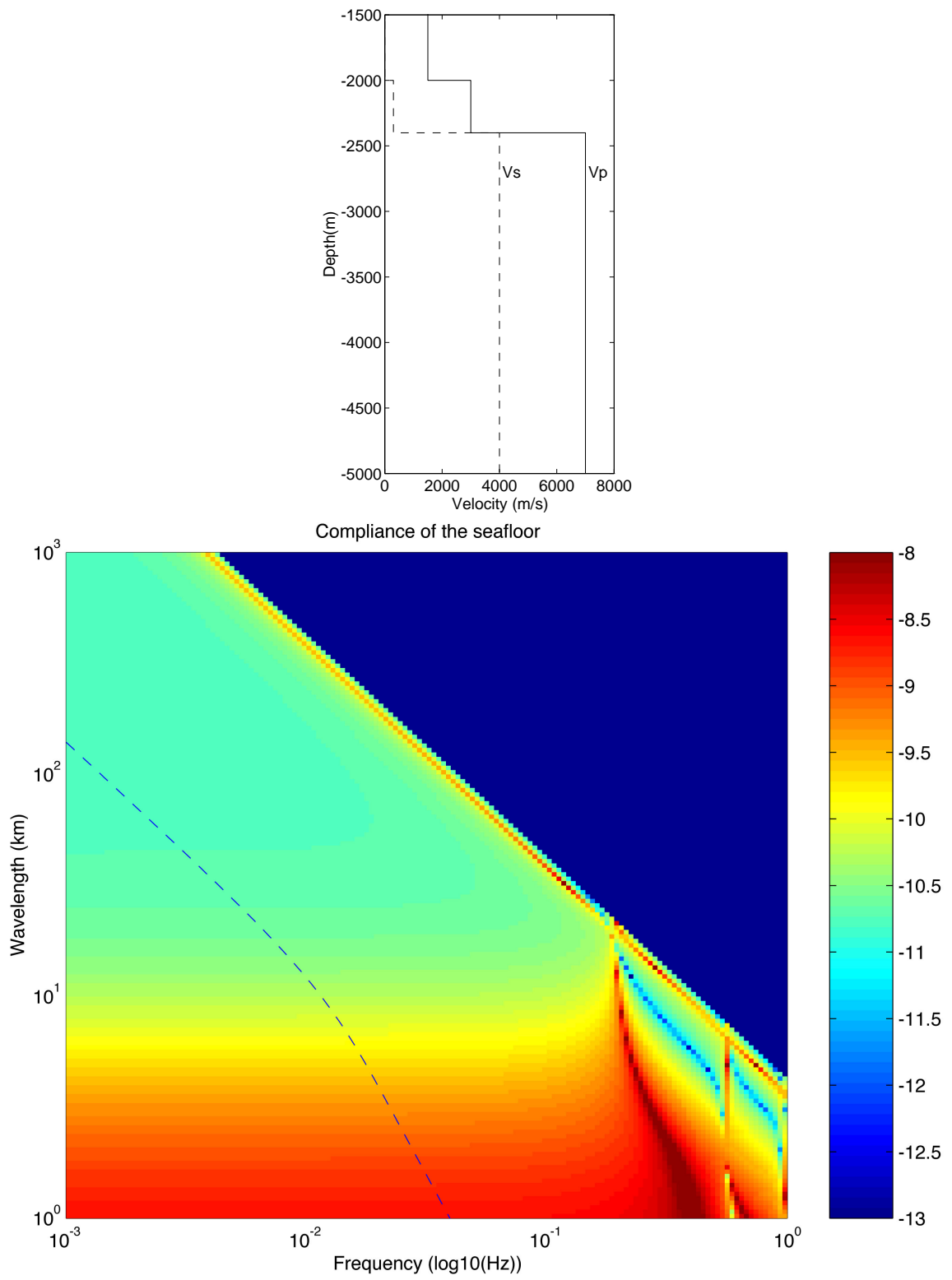


Figure 2.5: Compliance of sediments over a half-space

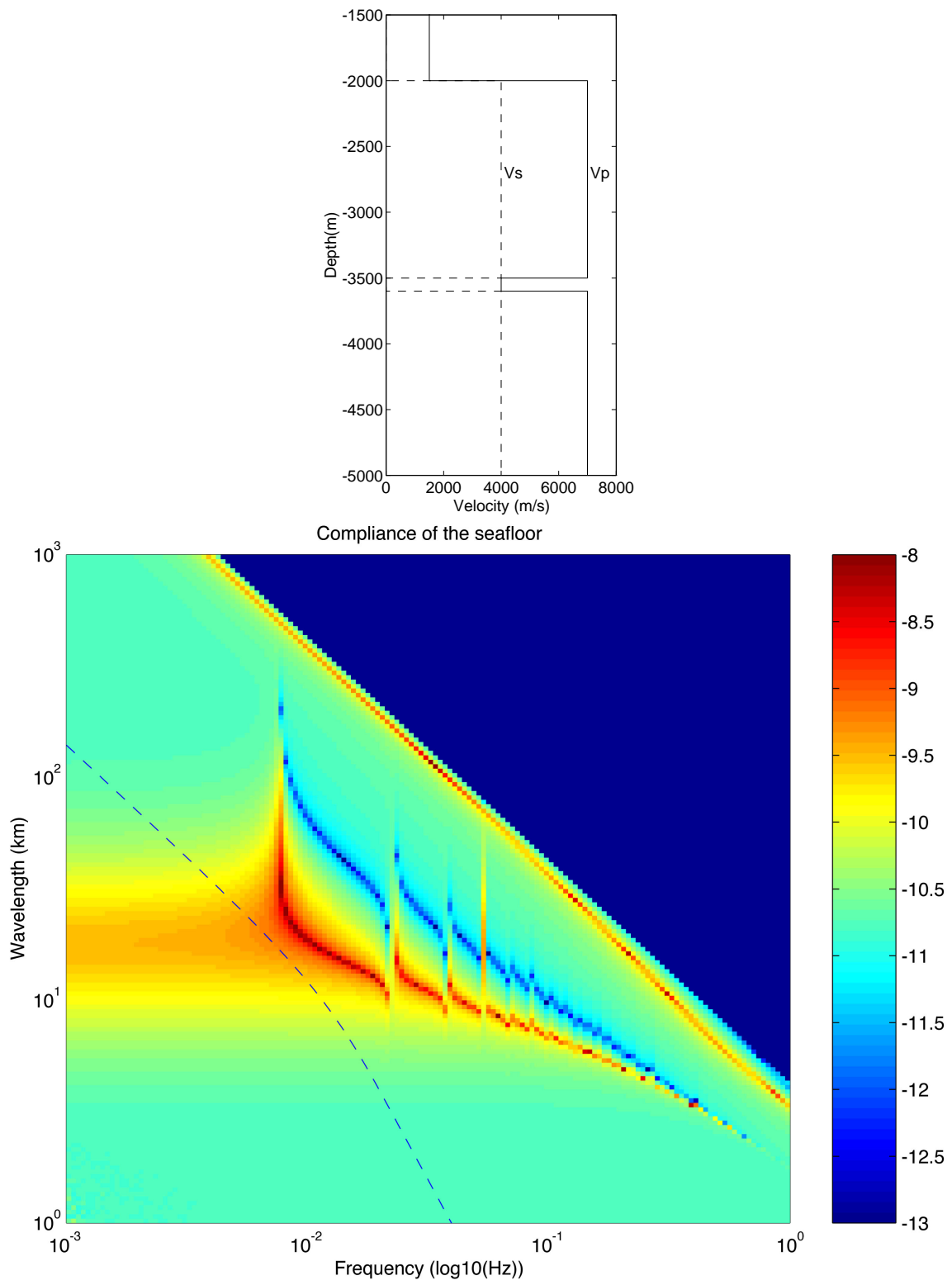


Figure 2.6: Compliance of a low shear velocity zone 1500 mbsf

allow determination of two elastic parameters instead of one. Unfortunately, horizontal displacements due to infragravity waves are smaller than vertical displacements, and even a noise-free horizontal long-period seismometer would have difficulty measuring horizontal acceleration between 20 and 300 seconds period, because seafloor water currents introduce noise comparable to the horizontal seismic levels. Positioning a horizontal sensor in a borehole has been suggested as a solution to this problem.

2.4 Appendix: Compliance of a Half-Space

Below is a derivation of the compliance of a half-space, following the method used by *Sorrels and Goforth* [1973]. Entering $\varphi = ae^{-rz}e^{i(\omega t+kx)}$, $\Psi = be^{-sz}e^{i(\omega t+kx)}$ into equations 2.9 and 2.11 gives

$$u|_{z=0} = i(ka - sb)\hat{x} + (kb - ra)\hat{z} \quad (2.23)$$

$$\tau_{zz}|_{z=0} = [(\lambda + 2\mu)r^2 - \lambda k^2]a - 2\mu ksb \quad (2.24)$$

$$\tau_{zx}|_{z=0} = \mu i [-2kra + (s^2 + k^2)b]. \quad (2.25)$$

Since $\tau_{zx}|_{z=0} = 0$,

$$b = \frac{2kr}{(s^2 + k^2)}a. \quad (2.26)$$

Substituting equations 2.24 and 2.25 in equation 2.1 gives

$$\xi_{hs}(\cdot) = \frac{kb - ra}{[(\lambda + 2\mu)r^2 - \lambda k^2]a - 2\mu ksb}. \quad (2.27)$$

Replacing b with a (using equation 2.26) and substituting ω^2/V_P^2 and ω^2/V_S^2 wherever possible (equation 2.19) results in:

$$\xi_{hs}(\cdot) = \frac{r\omega^2/V_S^2}{2\mu k^2 [2(k^2 - sr) - \omega^2/V_S^2] - (\lambda + 2\mu)(s^2 + k^2)\omega^2/V_P^2}. \quad (2.28)$$

Finally, we assume that $c \ll V_P, V_S$, and therefore (from equation 2.19) $r, s \rightarrow k$. To evaluate $(k^2 - sr)$, substitute for s and r using equation 2.19 and then use Taylor's expansion and cut off the higher order terms:

$$\begin{aligned} k^2 - sr &= k^2 - \left(k^2 - \frac{\omega^2}{V_P^2}\right)^{1/2} \left(k^2 - \frac{\omega^2}{V_S^2}\right)^{1/2} \\ &= k^2 - \left(k^2 - \frac{\omega^2}{2V_P^2} - \frac{\omega^2}{2V_S^2} + h.o.t.\right) \\ &\approx \frac{\omega^2}{2V_P^2} + \frac{\omega^2}{2V_S^2}. \end{aligned} \quad (2.29)$$

Substituting this result in equation 2.28 gives the compliance of a half-space under quasi-static forcing (equation 2.19):

$$\xi_{hs} = \frac{-\alpha^2}{2\beta^2 k \rho (\alpha^2 - \beta^2)} = -\frac{\lambda + 2\mu}{2\mu k (\lambda + \mu)}$$

Chapter 3

Seafloor Compliance Observed by Long-Period Pressure and Displacement Measurements

3.1 Introduction

Hello

Figure 3.1: West Cortez basin spectra and coherences

Figure 3.2: Axial Seamount spectra and coherences

3.2 Theory

Hello

Figure 3.3: Earth models and resulting compliances

Hello

Figure 3.4: Compliance sensitivity to shear velocity changes

Hello

3.3 Inversion

Hello

Figure 3.5: Compliance depth sensitivity

Hello

Figure 3.6: Inversions of model compliances

Figure 3.7: Effect of data uncertainty on inversion

3.4 Instrumentation

Hello

Figure 3.8: Axial Seamount and West Cortez Basin compliances

3.5 Measurements

Hello

Figure 3.9: Inversion starting models

Figure 3.10: Inversion results

3.6 Conclusions

Hello

3.7 References

Hello

This chapter, in full, is a copy of the material as it appears in *Journal of Geophysical Research* [1991]. The dissertation author was the primary author and researcher and the co-authors listed in that publication directed and supervised the research which forms the basis for this chapter.

Chapter 4

Crustal Aging at the East Pacific Rise, 9°50'N

4.1 Introduction

The East Pacific Rise (EPR) has been extensively studied by geologists and geophysicists because it is the fast spreading ridge (11.2 cm/yr at 9°N) closest to the United States. The ridge crest near 9°N is especially well studied due to morphological [*Haymon et al.*, 1993; *Macdonald and Fox*, 1988] and gravity anomaly [*Madsen et al.*, 1990] evidence that the 9°N segment has a strong magmatic supply. Numerous active seismic experiments have been conducted at the site, and intensive interpretation of the active seismic data [*Detrick et al.*, 1987; *Vera et al.*, 1990; *Toomey et al.*, 1990; *Christeson et al.*, 1992; *Harding et al.*, 1993; *Kent et al.*, 1993] has resulted in the most complete picture of mid-ocean ridge seismic structure to date.

The clearest picture of compressional velocity versus depth comes from “expanding spread profiles” (ESPs) [*Vera et al.*, 1990; *Harding et al.*, 1993].

Seismic data interpretations show a continuous axial magma chamber underlying the ridge. The magma chamber model consists of a thin (10-50 m) melt lens overlying a larger partially molten crystal mush zone which grades out to hot solidified rock [*Sinton and Detrick*, 1992; *Kent et al.*, 1993]. The melt lens width varies from 0.25 to 4 km along the 9°N segment, and is offset by minor ridge axis discontinuities.

Detailed shallow crustal compressional velocity profiles at 9°N are provided by *Harding et al.* [1993] and *Vera et al.* [1990]. *Harding et al.* [1993] find that layer 2A thickens over the first 1–2 km from the rise axis. Layer 2A is 0.2 km thick at the rise axis and thickens to 0.4–0.6 km through continuing extrusive volcanism within 1–2 km of the axis. Beyond this neovolcanic zone, *Vera et al.* [1990] find that – within the bounds of their expanding spread profiles (0–10 km off axis) — layer 2A thickens further with age, although they note that the across-axis increase in layer 2A thickness is no greater than along-axis variations in layer 2A thickness. Larger scale experiments [*Houtz and Ewing*, 1976] show that layer 2A thins with increasing age over the first 20–80 million years of crustal development. This thinning is interpreted as a result of closing and filling of pore spaces in the extrusive lavas by hydrothermal alteration. *Harding et al.* [1993] observe large variability and asymmetry of layer 2A thickness from 2–10 km off axis, but their data show no overall thickening of layer 2A beyond the first 1–2 km from the rise axis. The reason for the intermediate-scale

(0–10 km) thickening of layer 2A observed by *Vera et al.* [1990] is unexplained, and these results, if confirmed, would require off-axis constructional volcanism or alteration of young oceanic crust.

In May 1991, a series of experiments were conducted to probe crustal structure at 9°50'N on the EPR. In this chapter the results of three across-axis seafloor compliance measurements (figure 4.1) are discussed. The goal of the compliance measurements is to determine the shear velocity (V_S) structure of the EPR from 0–0.4 Ma (0–20 km off axis). Active seismic experiments usually directly measure only compressional velocity (V_P); V_S is inferred from assumptions about V_P/V_S or amplitude modeling. Seafloor compliance is especially sensitive to oceanic crustal V_S , augmenting V_P profiles by the greater sensitivity of V_S to crustal porosity and regions of partial melt within the crust.

The compliance measurement sites were chosen to cross the EPR at a local bathymetric high, corresponding to a local maximum magmatic budget. Reflection seismics [*Kent et al.*, 1993] place the top of the axial magma chamber approximately 1400 m below the seafloor at the axial high. The “ADVENTURE” expedition one month earlier at the same site found evidence — including burnt tubeworms and fresh lava — of a very recent eruption [*Hayman et al.*, 1993].

In addition to the compliance experiment, an active seismic experiment consisted of six airgun lines shooting to five ocean-bottom seismometer (OBS) positions, and a gravity survey including sea-surface gravity measurements using a shipboard Bell Gravity Meter (BGM-3) and seafloor gravity measurements using a deep ocean

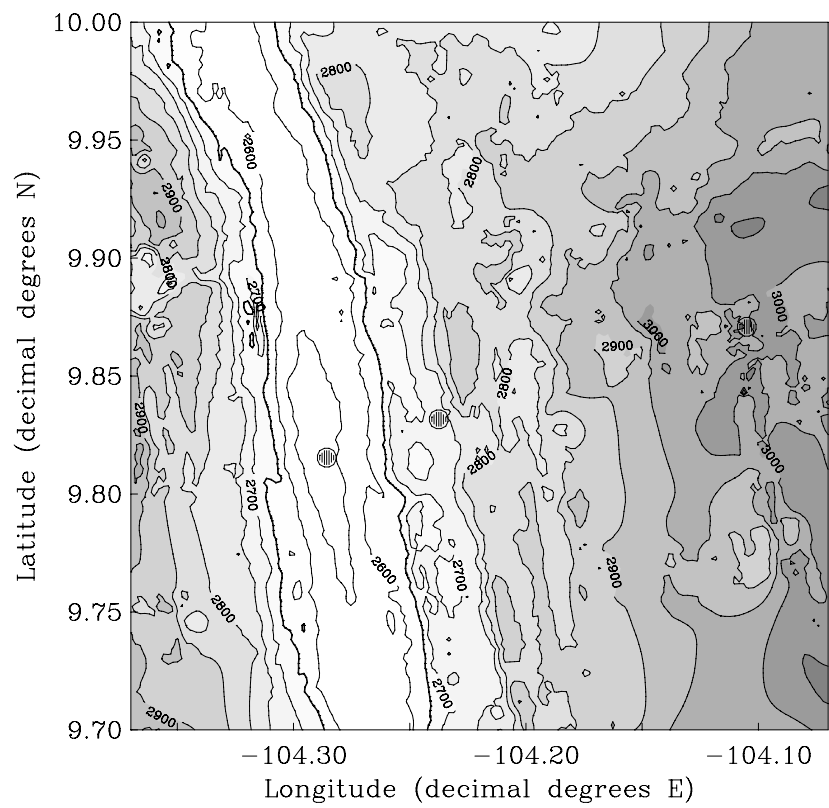


Figure 4.1: Bathymetry of the East Pacific Rise centered at $9^{\circ}50'N$. The seafloor compliance measurement sites (circles) are — from the ridge crest outwards — L-01, C-08, and C-01.

gravimeter [Hildebrand *et al.*, 1990]. As noted earlier, the compliance measurements compare seafloor acceleration (from the deep-ocean gravimeter) to stress (from a differential pressure gauge [Cox *et al.*, 1984]).

4.2 Measurements

We collected seafloor pressure and acceleration data at three sites on a line perpendicular to the EPR axis (figure 4.1). Site L-01 is located on top of the ridge axis maximum height, site C-08 is 5.6 km off axis (0.10 million years old (Ma) crust), and site C-01 is 20 km (0.37 Ma) off axis. Data are digitally recorded at 4 Hz. The length of each data record was four hours at C-01; three hours and thirty minutes at C-08; and one hour and ten minutes at L-01. Bad data segments caused by tugs on the gravimeter by its tether, rapid settling into mud or gravel, releveling episodes, and synchronization errors, are removed before spectra, coherences, and compliances are calculated using 2048-sample segments (approximately $8\frac{1}{2}$ minutes). Spacing between segments varies to avoid bad data episodes. Each segment is multiplied by a 4π prolate spheroidal window [Thomson, 1977] before application of the Fourier transform.

There are several possible error sources associated with estimating seafloor compliance from seafloor acceleration and pressure data. Instrument noise and seafloor motion due to sources other than seafloor pressure fluctuations (teleseisms, for example) are accounted for by including the coherence between the two instruments in equation 3.3. Instrument noise on the differential pressure gauge is believed

insignificant in the infragravity wave frequency band. The first one to two hours of acceleration data are dominated by instrument tilting as it settles into seafloor sediments. Data after the first two hours are less noisy, but the instrument is tethered to a ship on the surface, which effectively limits deployment times to a maximum of four hours. 17-minute-long (4096-point) windows optimize frequency resolution for spectral calculations, but the short deployment times force compliance calculations using $8\frac{1}{2}$ -minute (2048-point) windows to maximize degrees of freedom.

4.3 Analysis

Figure 4.2 compares compliances estimated from sites L-01, C-01, and C-08 (hereafter referred to as *measured compliances*) to compliances calculated from crustal models determined by the expanded spread profiles of *Vera et al.* [1990] (hereafter referred to as *V90 compliances*, figure 4.3). *Vera et al.* [1990] calculate density using the formula $\rho = 1.85 + 0.165V_P$ (V_P in km/s), and estimate V_S by assuming $V_P/V_S = 1.85$ everywhere except in the upper 200 m of crust, where seafloor reflection amplitudes require an increase in V_P/V_S to 2.4 at the surface. Uncertainties of the measured compliances are high because the short data sampling times allow few (7-15) windows for calculation of spectra.

The clearest feature of the measured compliances is the decrease in compliance with increasing age. Because compliance varies inversely with shear velocity of the crust, this trend corresponds to an increase in shear velocity with increasing age over the first 0.4 million years. The trend agrees with V90 compliances at frequencies

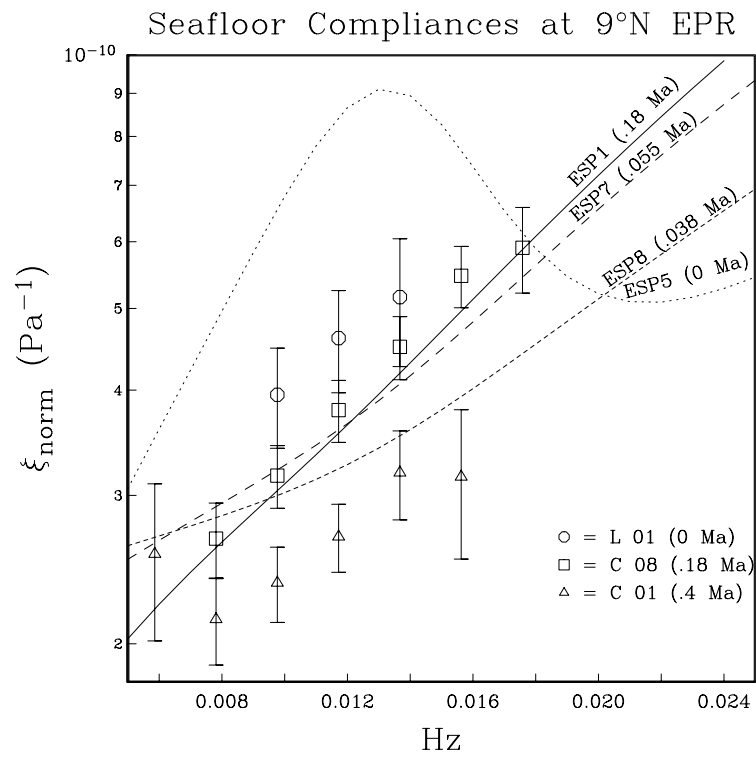


Figure 4.2: Compliances calculated from *Vera et al.* [1990] models (lines), and compliances estimated from seafloor pressure and acceleration measurements.

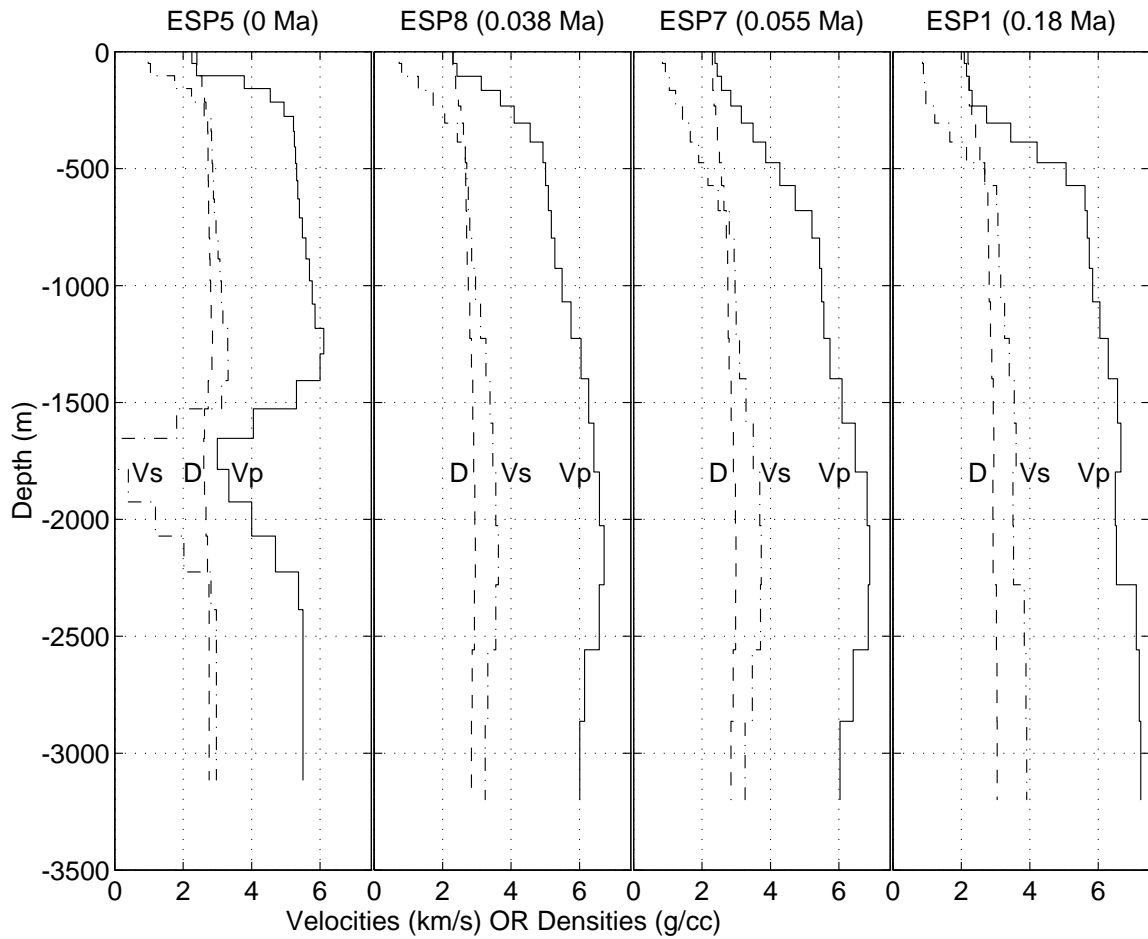


Figure 4.3: Crustal models at $9^{\circ}35'N$ on the EPR from expanding spread profiles (ESPs) of Vera *et al.* [1990]. V_s is shear velocity, V_p is compressional velocity, and D is density. Ma is estimated crustal age in millions of years.

below 0.008 Hz, but disagree with V90 compliances above 0.012 Hz. These high frequencies correspond to shallow depths, where *Vera et al.* [1990] model a decrease in V_P (an increase in layer 2A thickness) with increasing age. Seafloor compliance measurements decrease with increasing age at all frequencies, suggesting that layer 2A thickness decreases between the three sites. This contradicts the *Vera et al.* [1990] model of layer 2A thickening with increasing age beyond 2 km from the rise axis, and is consistent with the crustal aging models of *Houtz and Ewing* [1976].

High compliance observed at site L-01 (on axis) does not contradict the *Harding et al.* [1993] model of thin layer 2A within 1–2 km of the rise axis, because the high compliance probably is caused by the axial magma chamber. *Harding et al.* [1993] suggest that the extrusive layer thickens in the first 1–2 km from the ridge axis (0.02–0.04 Ma) due to continuing volcanic construction; after which shallow seismic velocities increase through hydrothermal alteration as the crust matures. A thin layer 2A results in a thin surface low-velocity zone, but the presence of a magma chamber creates a second low-velocity zone at depth. The thin layer 2A low velocity zone will decrease compliance at the highest infragravity wave frequencies, while the axial magma chamber increases compliance at slightly lower frequencies. Broad-band (0.005 to 0.025 Hz) compliance measurements can distinguish a magma chamber and a thin layer 2A, but the site L-01 data are too narrow-band in frequency to distinguish the two regions. Compliance estimates made using the autonomous gravimeter (chapter 5) allow a broader useful compliance frequency band with significantly lower data uncertainty.

Seismic wave attenuation data [Vera *et al.*, 1990] suggest V_P/V_S increases from the bottom of layer 2A to the seafloor. Seafloor compliance measurements should allow independent confirmation that V_P/V_S increases from the bottom of layer 2A to the seafloor. Figure 4.4 shows seafloor compliance estimated from site C-08 compared to compliances calculated from seafloor models based on ESP1, with different seafloor V_P/V_S ratios. One seafloor model is from ESP1, where $V_P/V_S = 1.85$ at 580 mbsf and increases to 2.41 at the seafloor. The second model assumes $V_P/V_S = 1.85$ throughout the crust. Most of the change in compliance is at frequencies above 0.02 Hz, which were not obtained using the tethered instrument but are within the range of the autonomous compliance sensor (see, for example, figure 6.3).

4.4 Inversion

Figure 4.5 shows shear velocity models constructed by inversion of compliance data from sites L-01, C-08, and C-01. The starting models use V_P and ρ estimates from Vera *et al.* [1990] ESPs, with site C-01 (0.37 Ma) using the same starting model as site C-01 (0.10 Ma), because the closest (in age) ESP to either of them is ESP1 (0.18 Ma). The inversion minimizes curvature of the resulting V_S model. Site L-01 compliance data can be fit with a single shear velocity value (no model structure). The shear velocity models at sites C-01 and C-08 are not significantly different, despite the considerable difference in compliance measured at the two sites. The higher velocities below 500 mbsf of site C-01 compared to site C-08

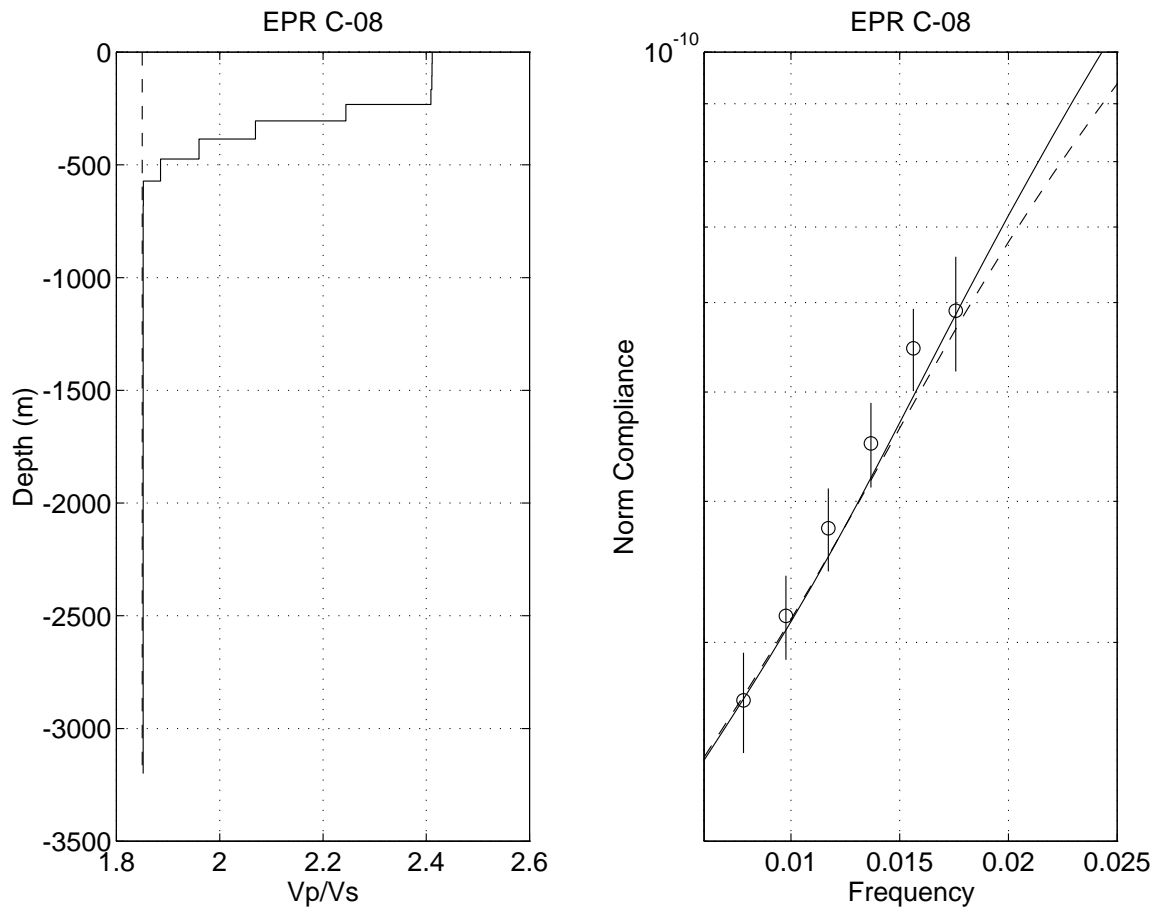


Figure 4.4: Compliances of site C-08 compared with compliances calculated from ESP1 (from *Vera et al.* [1990]) using different models of seafloor V_P/V_S .

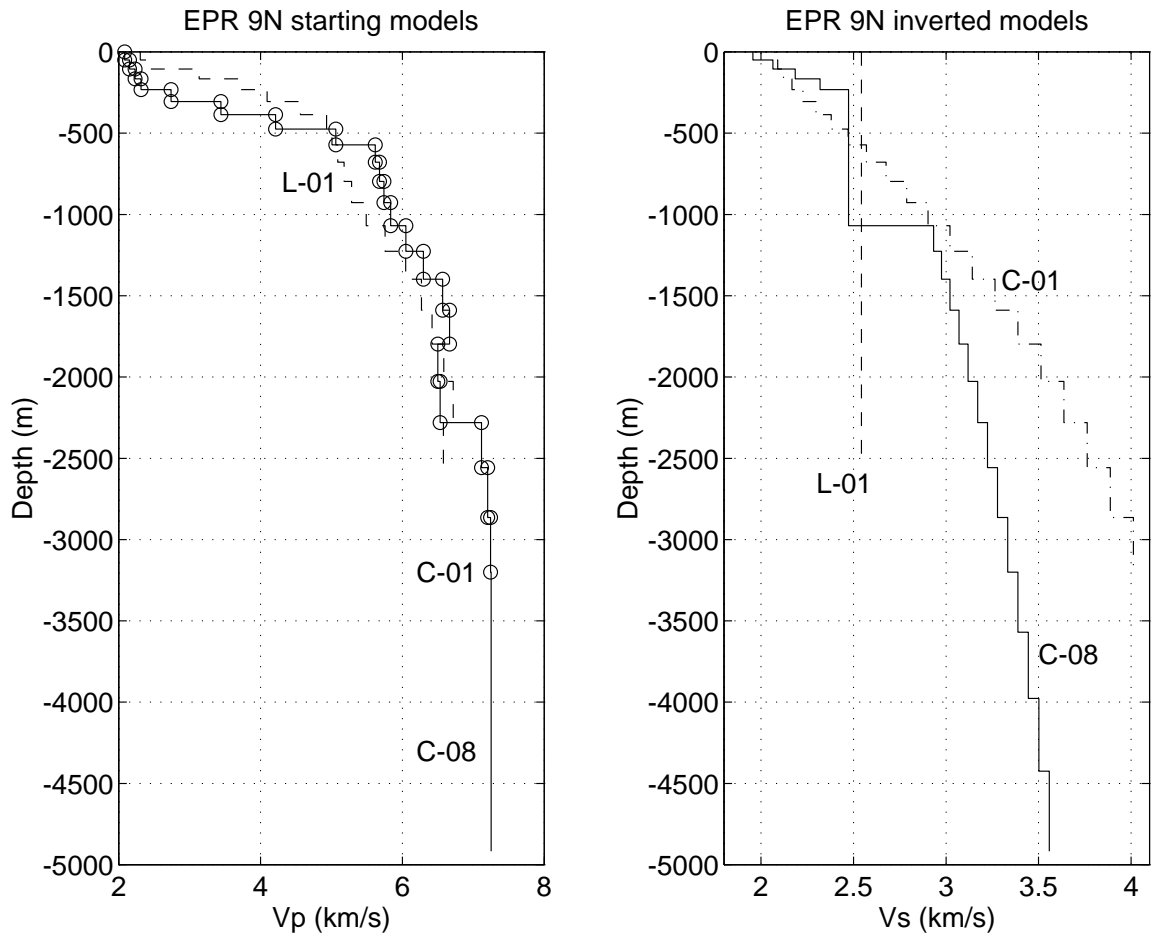


Figure 4.5: Shear velocity models constructed by inversion of EPR site compliances.

are sufficient to fit the approximately 30% lower compliance at the older site. This supports the qualitative assessment of the Analysis section that layer 2A thins with age within the first 20 km from the rise axis.

4.5 Conclusions

Seafloor acceleration and pressure time series are used to estimate seafloor compliance at three sites on the East Pacific Rise at $9^{\circ}50'N$. If we assume that the three sites represent typical young (less than 0.4 Ma) oceanic crust, two conclusions are reached:

1. Shear velocities in shallow young oceanic crust increase with increasing age. This effect comes primarily from aging of layer 2A. Crustal aging has been explained by: off-axis volcanism or infilling of cracks by sediments [Purdy, 1987], temporal changes in type of seafloor extrusion, basalt alteration, and precipitation of secondary minerals. Here it seems likely that precipitation of secondary minerals into thin cracks is the cause of the increase in shallow crustal velocities with age. *Harding et al.* [1993] found that layer 2A thickens in the first 1–2 km, a result which is not within the resolution of this compliance experiment. Compliance is higher at 0.0 Ma than at 0.1 Ma, which might seem to contradict the assertion of thin layer 2A at 0.0 Ma, but the signal is probably dominated by the axial magma chamber.
2. Data inversions can be improved by decreasing data uncertainty. Compliance data from the tethered gravimeter do not extend to high enough frequency

to determine the V_P/V_S ratio in the uppermost crust, but compliance data from long seafloor deployments (such as the deployment at West Cortez Basin in chapter 3) are broader band and have smaller uncertainty. An experiment using the autonomous deep-ocean compliance sensor (chapter 5) should be able to constrain the depth of the axial magma chamber.

Chapter 5

An Autonomous, Deep-Ocean, Compliance Sensor

5.1 Introduction

Specialized instruments are needed to determine seafloor pressure and displacement in the frequency range of seafloor compliance measurements (0.003–0.04 Hz). We use differential pressure gauges [*Cox et al.*, 1984] to measure the pressure signal, and a LaCoste-Romberg underwater gravimeter [*Lacoste*, 1967] to measure seafloor acceleration. The gravimeter works as a long-period seismometer with a useful frequency range two decades lower than typical ocean-bottom seismometers.

Seafloor compliance measurements were originally performed using a tethered instrument lowered from a research vessel. The research vessel was required to hold station within 50 meters of the lateral position of the measurement site.

Tethered instrument data usually have several data glitches caused by tugs on the instrument through the tether, and the longest compliance measurement obtained using this technique lasted only four hours. Longer measurements (24 hours or more) are preferred in order to maximize degrees of data freedom, and because the first one to two hours of data are dominated by noise from the instrument settling into sediments and from differential pressure gauge thermal equilibration. The tethered gravimeter provides real-time data acquisition and instrument control, allowing rapid response to seismometer problems including fish bumps, tidal drift of gravity, settling into sediments, instrument failure, instrument calibrations, and a “sticky” seismometer beam. However, robust control software and hardware can perform all of these tasks almost as well as a human operator.

We designed an autonomous, deep-ocean compliance sensor (ADOCS, figure 5.1) to improve seafloor compliance measurements by allowing multiple-day deployments while minimizing use of ship time. Multiple-day deployments allow rejection of data during periods of low pressure-acceleration coherence caused by seismic events, instrument settling, and incidence of forced infragravity wave energy on the seafloor. To obtain acceptable frequency resolution in the compliance frequency band, long (17-minute) windows are used to calculate compliance. Several hours of data must be collected to obtain the large number of degrees of freedom in the calculated spectra necessary to adequately constrain the compliance values. The best constrained compliance data collected using the tethered gravimeter is from an experiment where the instrument was deployed for 24 hours from a stable instrument

Figure 5.1: The autonomous deep-ocean compliance sensor.

platform.

5.2 ADOCS overview

The most important objectives in designing the software and hardware of the autonomous deep-ocean compliance sensor were to operate and protect the LaCoste-Romberg underwater gravimeter used for seafloor acceleration measurements. Specific design features of the ADOCS are:

1. To support two modes of operation. An autonomous mode controls the instrument during seafloor deployment, and an interactive mode is used for testing in the laboratory. The interactive mode also allows the tethered instrument to use the same control program, taking advantage of software design improvements.
2. To be able to save data inside the instrument or send the data out a serial port in real time (*uplink* mode) to the user. Saving onboard is necessary for autonomous operation, while sending data uplink is important for testing, verifying data saved onboard, and using the instrument as a tethered gravimeter.
3. To protect the delicate gravimeter beam using software and hardware controls. Accelerations of 3 milligals (approximately $\frac{1}{330,000}$ th gravitational acceleration) can damage the beam by driving it into the top or bottom stop. A motor-driven system in the sensor protects the beam by gently clamping it against the bottom stop when the gravimeter is not in use. We developed software and hardware routines to clamp the gravimeter beam when the instrument is

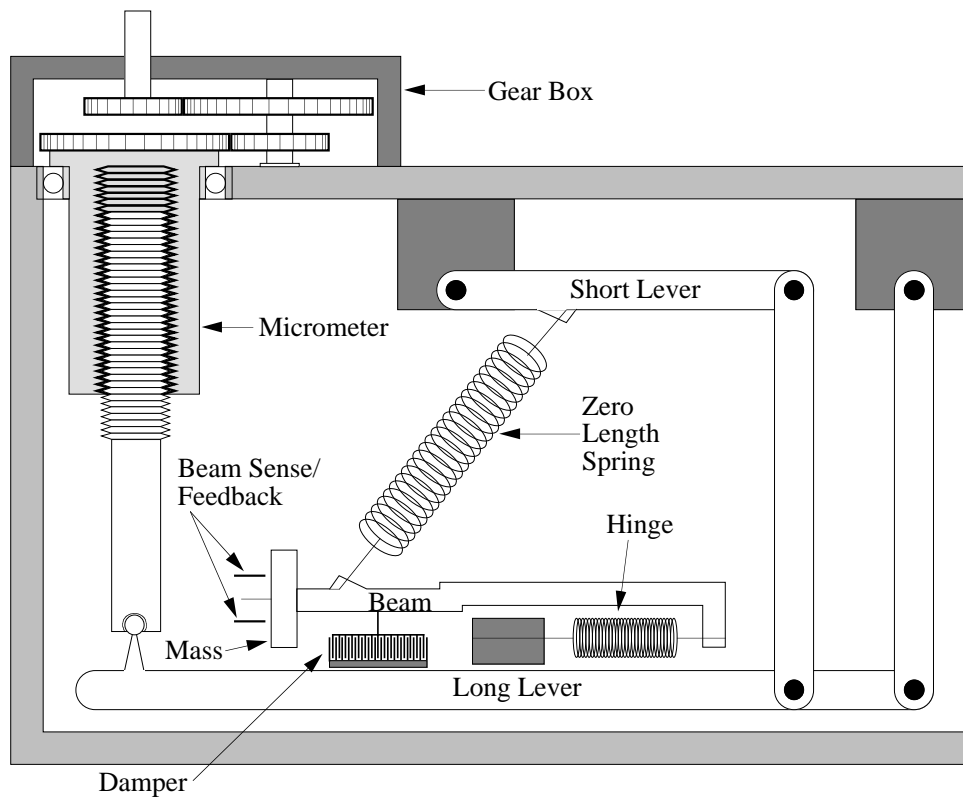


Figure 5.2: Simplified drawing of the inside of a Lacoste-Romberg gravimeter, modified from the *Model U Underwater Gravity Meter Instruction Manual*, by Lacoste-Romberg, 1990.

jostled or acceleration data are not being collected (between experiments, and during instrument deployment, thermal equilibration, and recovery).

4. To maintain the gravimeter beam near the center of its range. This maximizes linearity and allows large signals to be sensed without clipping. The beam is centered by adjusting the top end of the instrument spring using a micrometer screw and a series of levers (figure 5.2).

5. To keep the gravimeter nearly level, since 1) the measured acceleration signal is the true acceleration signal times the cosine of the deviation from level and 2) the frequency response characteristics of the sensor are affected by any deviation from level.
6. To have accurate instrument timing, so that arrival times of teleseismic earthquakes can be determined.
7. To be able to calibrate the acceleration sensor and differential pressure gauge while the instrument is on the sea floor.
8. To use two redundant differential pressure gauges (DPGs) for various data quality and instrument calibration functions. The coherence and transfer function between the two gauges are used to verify the assumption of insignificant noise on the pressure gauges, and to confirm calculated frequency response of the gauges. Also, one gauge measures the background seafloor pressure signal while the other gauge is being calibrated.
9. To minimize power consumption, since all power is carried inside the instrument.

The ADOCS consists of electronics and a Lacoste-Romberg gravimeter inside a pressure housing placed inside a frame supporting other instruments and launch/recovery apparatus (figure 5.1). The pressure housing consists of two 25" outer diameter (O.D.) machined aluminum hemispheres on a 25-3/4" O.D. machined

aluminum center ring. The center ring has five electrical feed-throughs and one pressure port. Inside the pressure case (figure 5.3) are an electronics card cage, a platform for batteries and acoustic transducer cards, and a 9-1/2" O.D. ceramic sphere containing the LaCoste-Romberg gravimeter and its feedback and signal amplification electronics. The inner sphere is gimbaled, with level sensors inside the sphere and leveling motors on the gimbals. The pressure housing sits in a hexagonal frame made of square aluminum tubing. Two differential pressure gauges (DPGs) are mounted on the frame along with solenoids for DPG calibration, two hydrophones for acoustic ranging and release of the instrument, two 70-pound drop weights on burn wires, and an absolute pressure gauge. The frame is covered by three large polyethylene panels to protect the hemispheres, connectors, and external gauges. Five 12" glass floats provide flotation.

The Lacoste-Romberg gravimeter, invented by Lucien Lacoste in 1935, obtains low-frequency seismic measurements without the need for a large mass. Standard pendulum seismometers (figure 5.4) have a natural frequency equal to $\sqrt{k/M}$, where k is the spring constant and M the mass. Using this system, a large mass is required to measure low-frequency seismic energy. The Lacoste-Romberg gravimeter uses a different geometry in which a precise balance of m , k , and the pendulum system dimensions h_1 , h_2 , and h_3 (figure 5.4) and use of a *zero-length spring* (the force-length plot passes through the origin), results in a zero natural frequency. The system can become unstable with any variation in system dimensions or spring constant, so the pendulum is detuned to have a non-zero natural frequency. The IDA

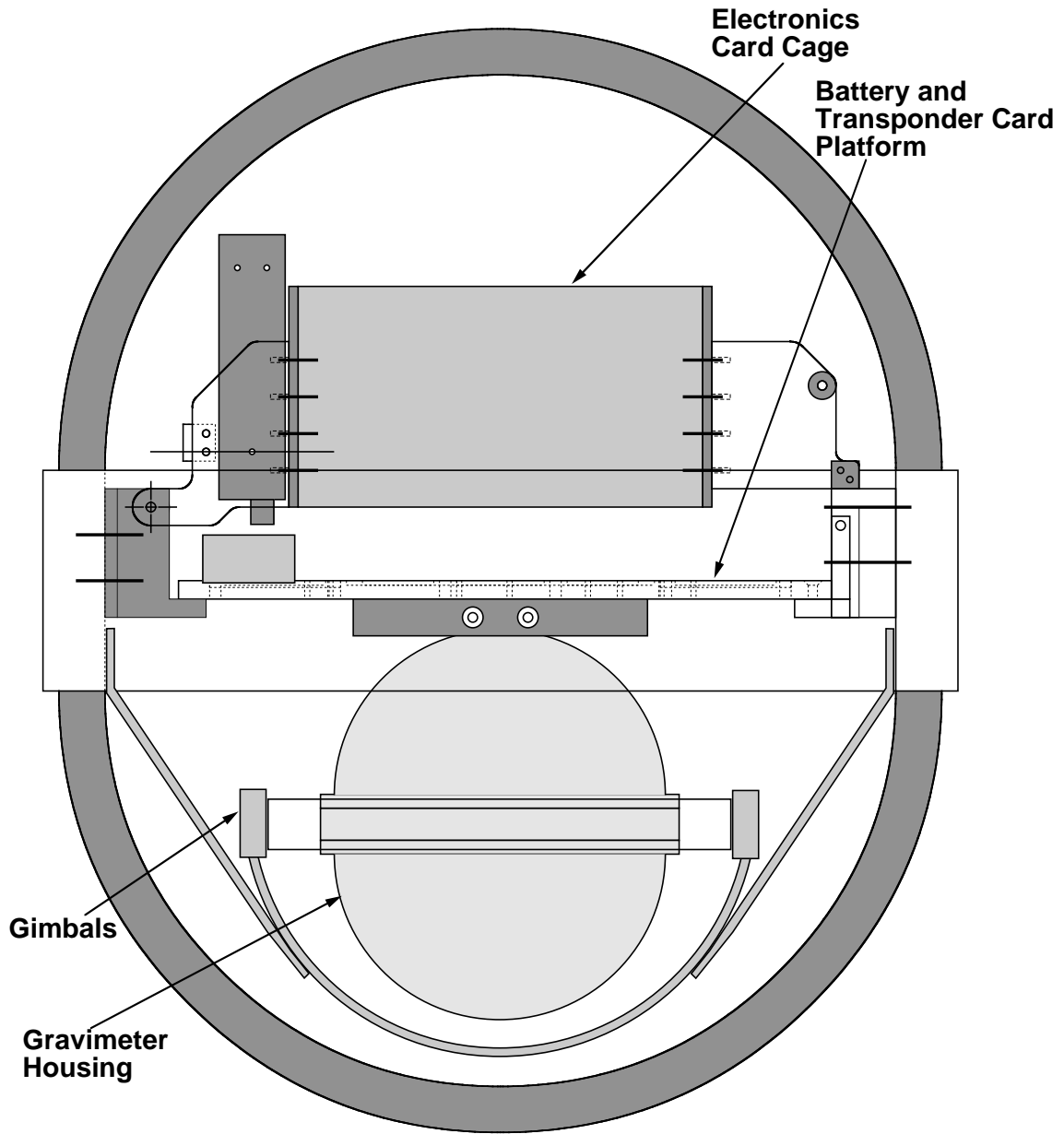


Figure 5.3: An view inside the autonomous compliance sensor pressure housing.

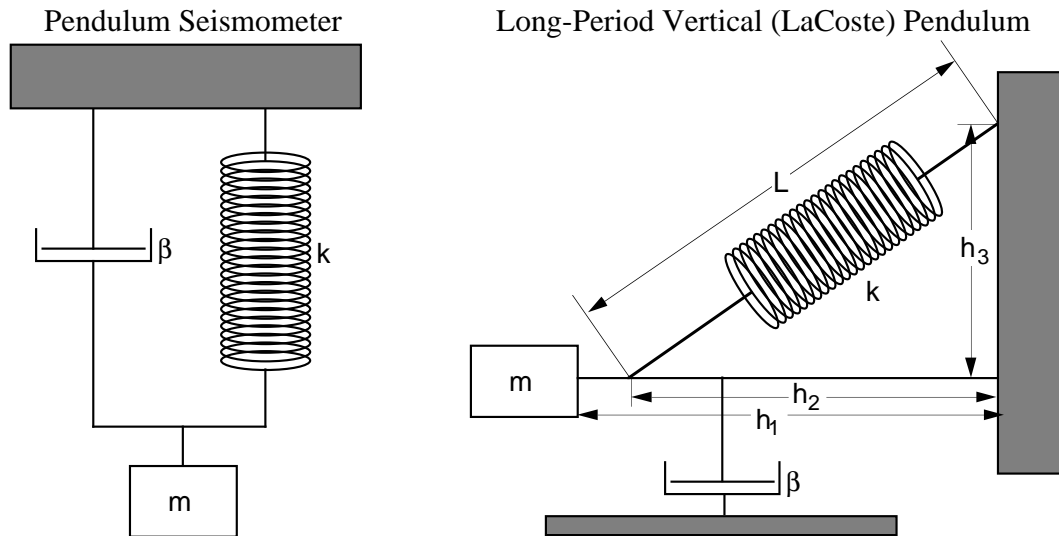


Figure 5.4: Basic components and important parameters of a pendulum seismometer and the Lacoste-Romberg vertical pendulum.

(International Deployment of Accelerometers) network of Lacoste-Romberg gravimeters is tuned to a natural period of 10 seconds. Because the frequency response is very sensitive to the spring constant, the spring is maintained at constant temperature using a feedback-controlled heater. Lacoste-Romberg underwater gravimeters also use capacitive plates to sense and apply feedback to the gravimeter beam. The beam feedback, which must be tuned to maintain critical damping, increases the usable frequency range of the gravimeter and reduces the beam travel to increase linearity of the instrument response.

To optimize the frequency response of the Lacoste-Romberg gravimeter, the long level (which controls rotation about the beam axis) is adjusted until the response has infinite period. This is tested by turning capacitive feedback off and

pushing the beam away from the center position. If the beam stays at the new position rather than returning to the center position, the instrument has infinite period. For stability purposes, the long level is then adjusted to slightly less than infinite period. Once the proper level value is determined, the feedback is adjusted to eliminate resonance, which can occur at the feedback system lowpass cutoff frequency (0.1 Hz for the ADOCS gravimeter). Any change in level from this position modifies the feedback–damping relationship, resulting in overdamping or underdamping.

The Lacoste-Romberg gravimeter in the ADOCS is slightly different from the one used in the tethered instrument. The tethered instrument’s gravimeter has one pair of capacitive plates at the end of the beam to sense beam position and to provide feedback. The gravimeter in the autonomous instrument has two pairs of capacitive plates; a pair of sensing plates positioned at the end of the beam and a pair of actuating plates providing feedback at the center of mass of the beam. Unfortunately, the actuating plates have only half the capacitance of the sensing plates, allowing more noise to enter the system. We use the “sensing” plate for both sensing and actuation, as in the tethered instrument. The ADOCS gravimeter spring is zero-length at 17.05°C with a broad “nose” (that is, it is not sensitive to temperature fluctuations from about 15°C to 19°C). By comparison, typical Lacoste-Romberg underwater gravimeters are most stable at 54°C ; with a heater maintaining the nose temperature. Power considerations preclude heating the ADOCS gravimeter for multiple-day deployments, fortunately deep seafloor temperatures are stable enough to eliminate the need for a heater. When testing the instrument in the lab-

oratory, meter temperature is maintained at $30.00 \pm 0.01^\circ\text{C}$ by a linear temperature regulator.

5.3 ADOCS hardware

The autonomous compliance sensor is controlled by a CMOS 8088 microprocessor on a commercial CPU card that plugs into a C-44 bus along with a parallel controller card, a serial port controller, a memory card, a SCSI interface card, and a card for interfacing with the data collection A/D. The memory card has three 128-kilobyte RAM chips and a 128-kilobyte EPROM that contains the instrument control program. The differential pressure gauge outputs are sensed by pressure cards [Cox *et al.*, 1984], and all analog signals are converted to digital signals by multiplexing into the A/D converter. Three specialized cards were designed for the autonomous gravimeter:

Parallel interface and shaft encoder control: This card connects the inputs and outputs of the CPU parallel ports to the gravimeter (inputs include an instrument flood sensor and beam clamp status switches; outputs include motor controls and gravimeter beam feedback mode selector). The card also contains hardware to decode signals from a shaft encoder on the gravimeter spring position micrometer and translate them into micrometer turns, which can be input through the parallel port.

Fail-safe clamp Clamps the gravimeter beam if the computer program stops running or the instrument drop weights are released.

Power and solenoid Contains voltage regulators to generate voltages for other cards using ± 15 V supplied from the batteries. This card also stores 40 V on two capacitors that drain into solenoid lines used for calibration of the differential pressure gauges.

5.4 ADOCS software

Figure 5.5 is a flowchart of the computer program that controls the autonomous compliance sensor. The software supports saving data onboard to a disk drive, sending data to a serial port, or both. The software also has interactive and autonomous control modes. In the interactive mode, the user sends commands to the instrument over a serial line. In the autonomous mode, the instrument follows a schedule describing when to calibrate the differential gauge, when to start leveling, and when to start measuring seafloor accelerations. In either mode, the program can automatically level the gravimeter or unclamp the beam and adjust the micrometer screw to center the beam. Figure 5.6 is a flowchart of the releveling operation, while figure 5.7 outlines the gravimeter micrometer screw adjustment. The control program relevels the instrument and/or adjusts the micrometer screw synchronously with performing its other functions by calling the level or micrometer screw subroutine whenever the A/D processes a new data block (every $\frac{1}{8}$ second). The subroutines perform one brief action (turning on a motor, decrementing response time counters), save status in global variables, and return control to the main program until they are called again $\frac{1}{8}$ th second later.

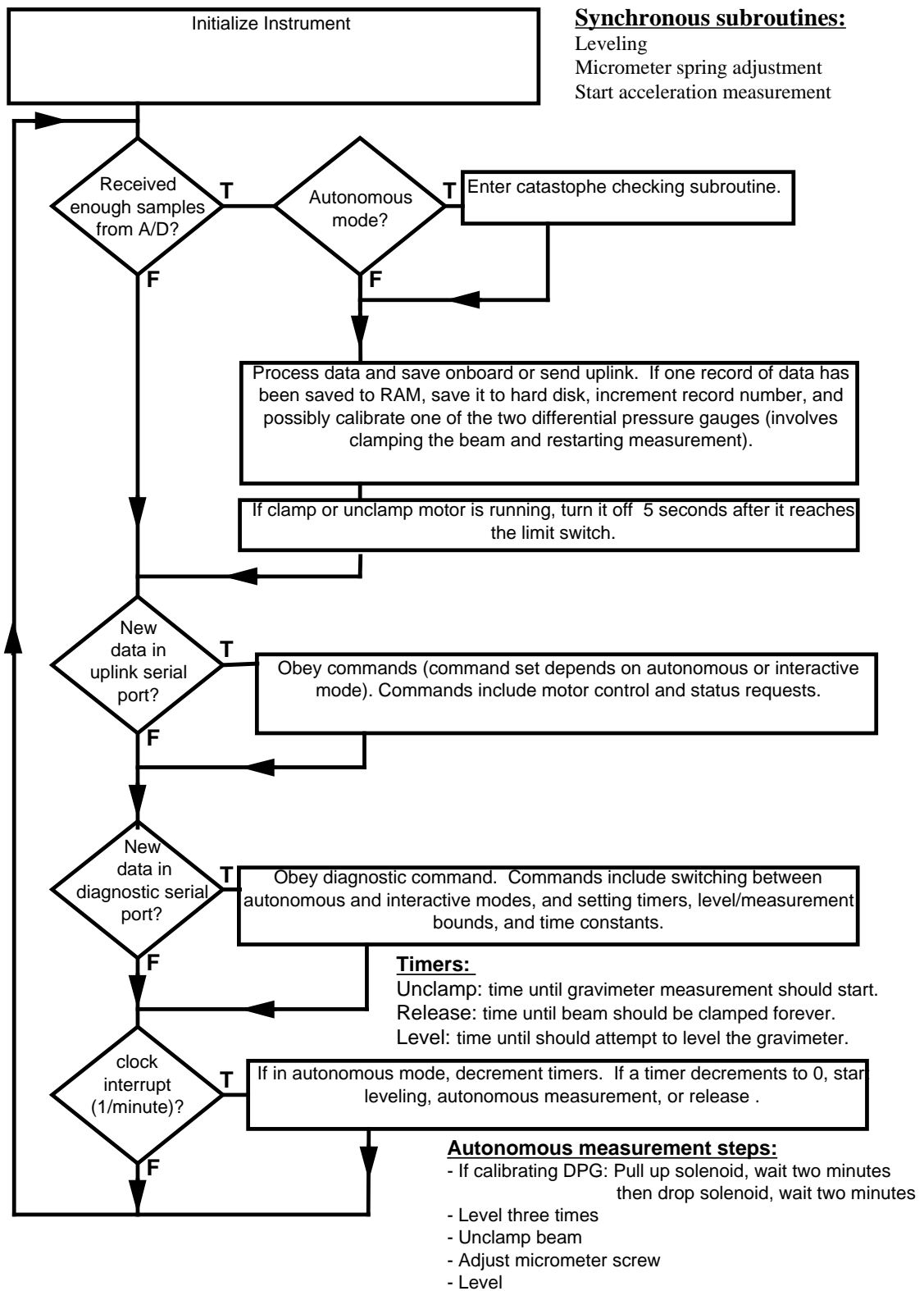


Figure 5.5: Autonomous compliance sensor control program.

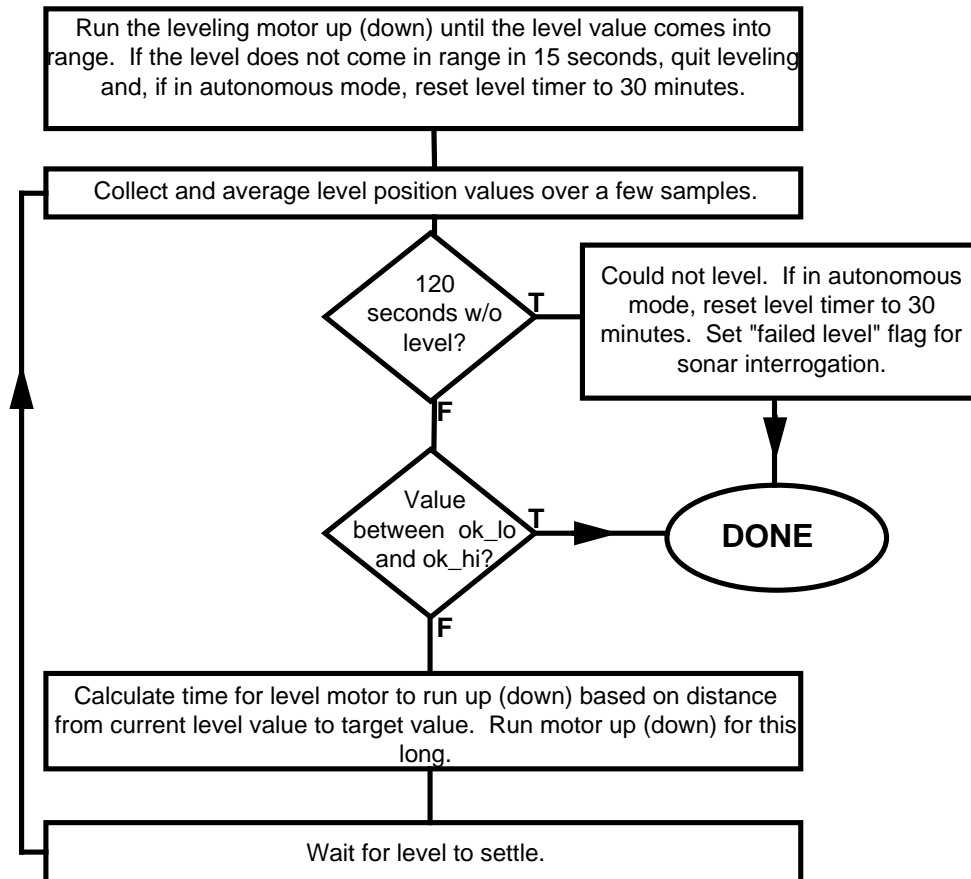


Figure 5.6: Autonomous compliance sensor automatic leveling subroutine.

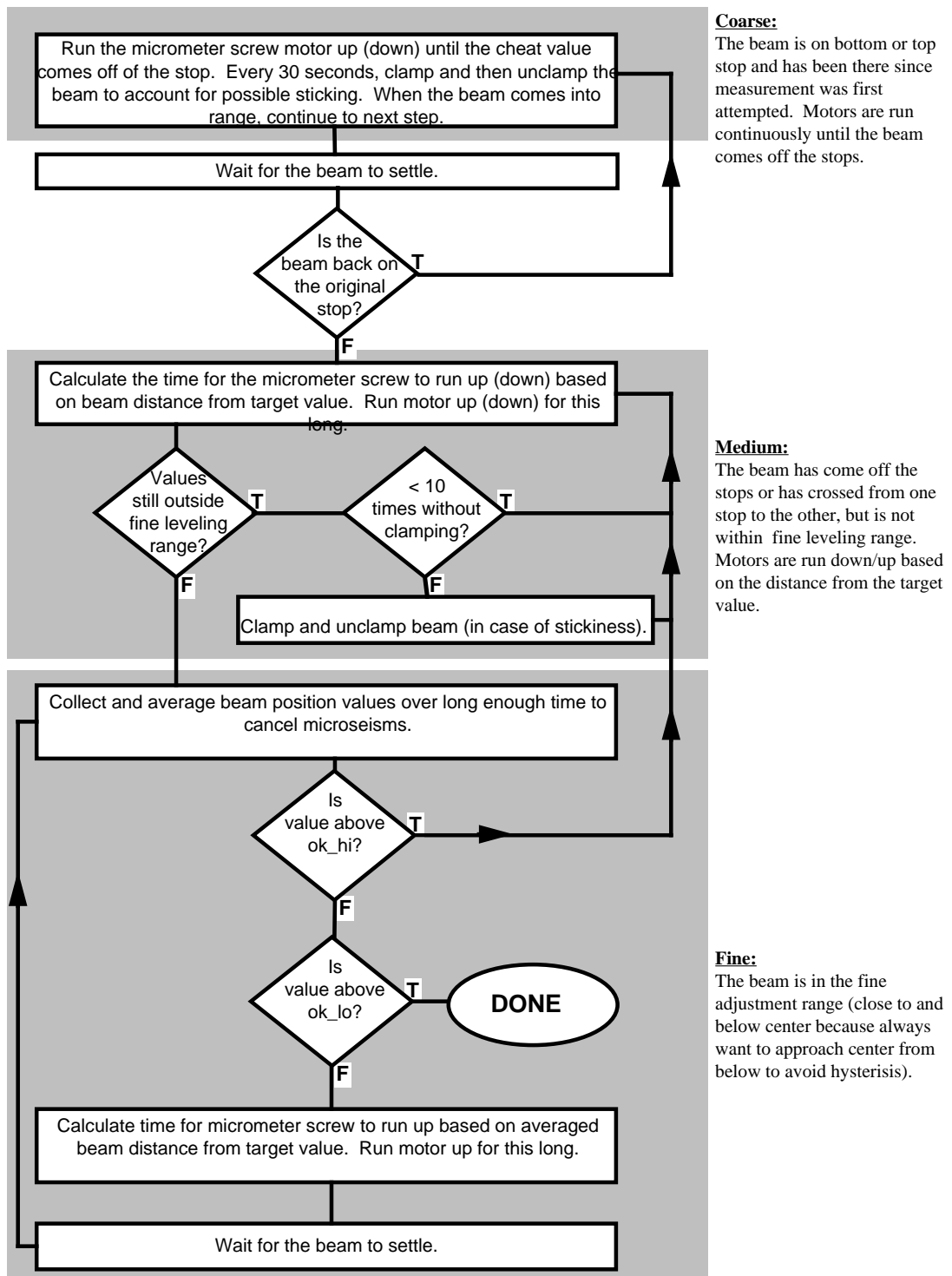


Figure 5.7: Autonomous compliance sensor automatic measurement subroutine.

In autonomous mode, the control program decrements level, beam unclamp, and instrument release timers on once-per-minute clock interrupts from an 80C58 Real-Time Clock. Once the beam has been unclamped, the program determines if the beam must be clamped (due to rapid changes in levels or beam position) or if the levels or micrometer screw should be adjusted (figure 5.8). The instrument timers, clock, and micrometer spring and leveling motor timing parameters can be adjusted using a 19200 baud serial diagnostics port. Before each deployment, instrument timers are reset using this port. After instrument recovery, the diagnostics port is used to upload data from the instrument to a backup disk drive. When the instrument is to be deployed several times during one expedition, the 128-kilobyte EPROM on the memory card is replaced with a 128-kilobyte RAM memory chip, onto which the control program is loaded. The RAM chip allows the control program to be modified (via the diagnostics port) between deployments without opening the pressure housing.

The ADOCS can also function interactively. Interactive control allows the ADOCS to be tested and adjusted in the laboratory. Up/downlink communication uses a 2400 baud serial link. ASCII control codes are sent to the instrument, and binary data is sent from the instrument as 14 2-byte channels at an overall data rate of 4 Hz. The diagnostics port can be used for instrument debugging.

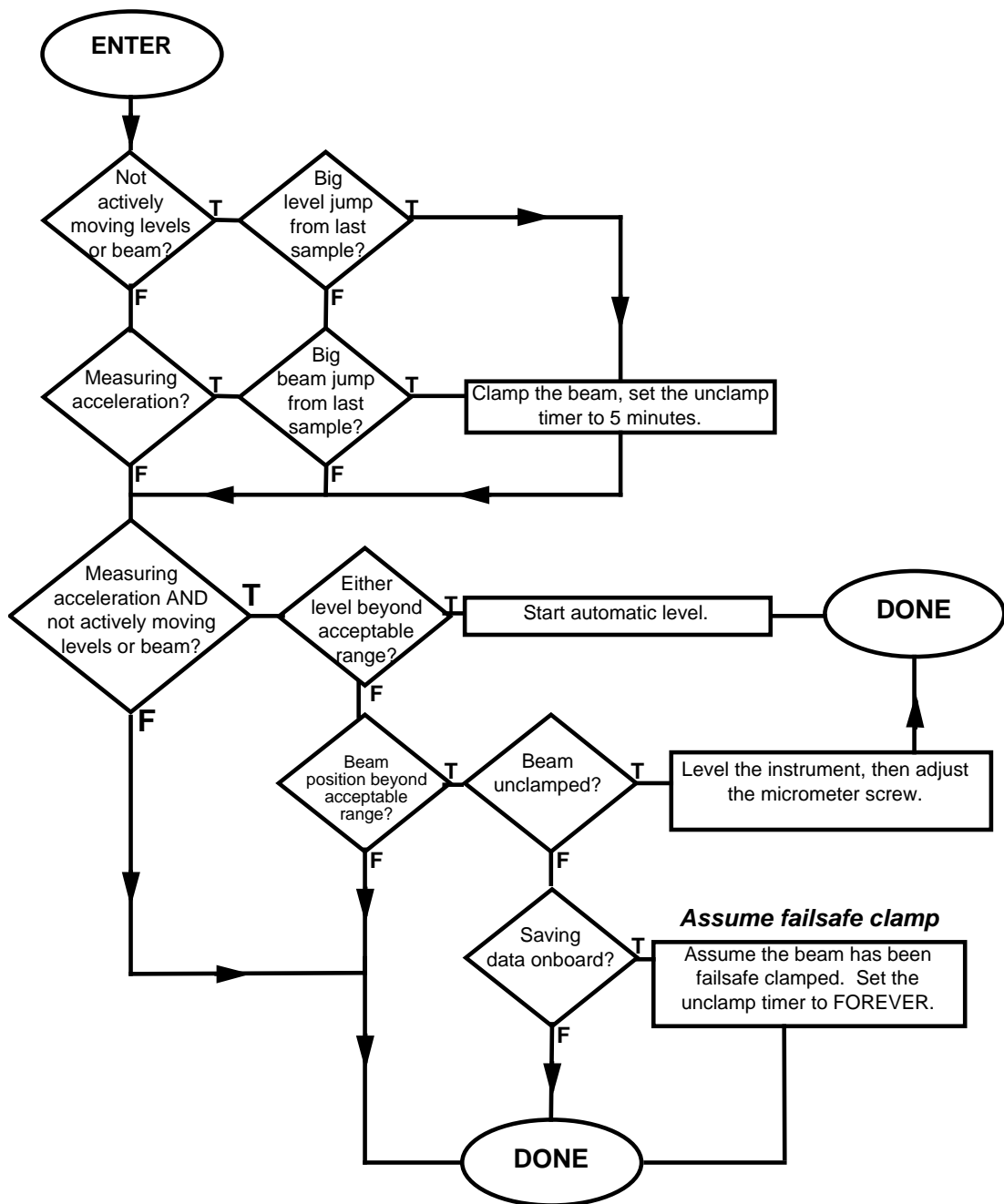


Figure 5.8: Autonomous compliance sensor “catastrophe” subroutine.

5.5 ADOCS mechanicals

5.5.1 Noise sources

There are several potential sources of noise on the gravimeter, including electronic noise and thermal effects. Electronic noise is only significant on the DPGs in the noise notch just above the infragravity waves (0.02–0.1 Hz in figure 6.2) because of the large pressure signal amplitude at higher and lower frequencies. Electronic noise could provide a low-frequency limit for the gravimeter data, but thermal noise currently dominates below about 600 seconds period. Electronic noise can be avoided by increasing the low-frequency output gain of the gravimeter or by using a more stable voltage reference.

The Lacoste-Romberg gravimeter is sensitive to temperature fluctuations as small as 0.01°C . The farther away the instrument temperature is from the spring's nose temperature, the more temperature sensitive the instrument is. Variations in room temperature ($\approx 27^{\circ}\text{C}$) cause a large (full range in one minute) beam drift in the uninsulated ADOCS gravimeter (nose temperature = 17°C). To dampen the ambient temperature signal, the gravimeter sits inside a 9-1/2" O.D. ceramic sphere stuffed with cotton insulation. The ceramic sphere sits within a 25" O.D. spherical aluminum pressure case. Upon deployment, the ADOCS gravimeter takes approximately 18 hours to equilibrate to seafloor temperatures (figure 5.9), and the differential pressure gauges take approximately four hours. More efficient insulation and replacement of metal connections that penetrate the ceramic sphere would dampen the external temperature signal even further, but would also increase the time necessary for initial

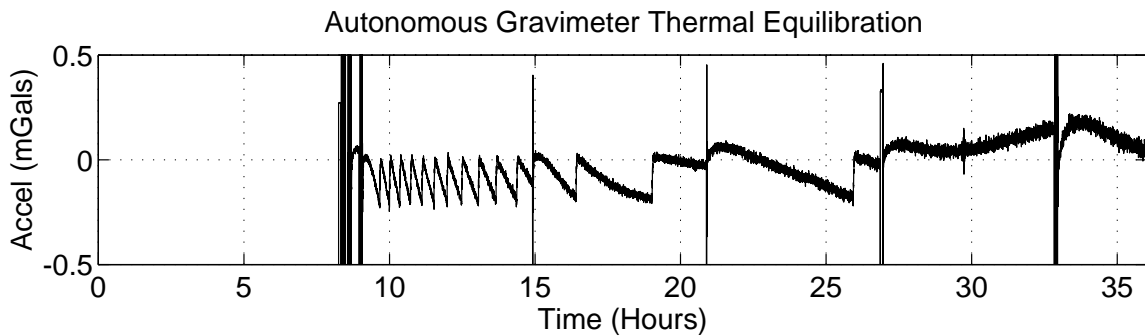


Figure 5.9: Acceleration signal from first 36 hours of autonomous gravimeter deployment. The beam was clamped for the first eight hours. Breaks in data every six hours are from beam clamping during transfer of data to hard disk. The energy at 29-30 hours is due to teleseismic energy from a magnitude 5.5 earthquake in the Eastern Sea of Japan.

thermal equilibration.

A May 1993 experiment on the Floating Instrument Platform (FLIP) compared noise levels on the ADOCS and a heated Lacoste-Romberg underwater gravity meter. The two instruments were bolted together and lowered on a tether to 1700-meter-deep seafloor from FLIP for one 36-hour deployment. The acceleration power spectra from the two instruments (figure 5.10) indicate that the autonomous gravimeter (unheated) has a higher noise level level at the lowest frequencies, but that the heated gravity meter noise signal is more broadband, and masks the acceleration signal at higher frequencies. The heated instrument's low-frequency noise is probably a result of the gravimeter heater feedback control, which prevents large temperature fluctuations, but creates higher frequency temperature fluctuations associated with the feedback delay. We conclude that — after one day of thermal equilibration — the unheated gravimeter obtains better compliance estimates than the heated version.

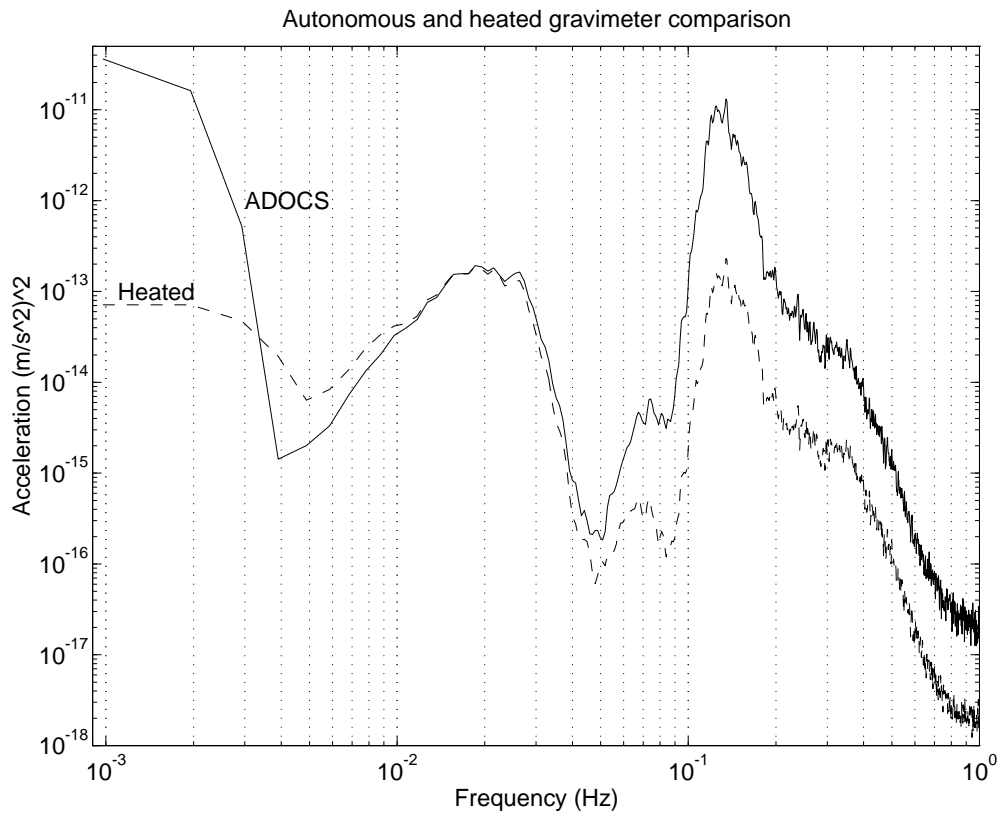


Figure 5.10: Acceleration spectra comparison between the ADOCS and the tethered gravimeter. The two spectra have different shapes because the ADOCS gravimeter beam feedback voltage was adjusted to give a resonance at 0.1 Hz.

This result is valid at seafloor sites with small temperature variations (probably $< 0.02^{\circ}\text{C}$) over periods less than 500 seconds.

5.5.2 Calibration

ADOCS sensors are calibrated on the seafloor because both the LaCoste-Romberg gravimeter and the differential pressure gauge gains and frequency responses depend on ambient temperature. Temperature affects the DPGs by changing the viscosity of the gauge oil and by changing the resistances in the strain gauges used to measure pressure variations. The strain gauge signal is highpass filtered by a capillary tube connecting the gauge reference chamber to ambient pressure. The time constant of this high-pass filter depends on the diameter and length of the tube and the temperature- and pressure-dependent viscosity of the mineral oil. Furthermore, an increase in hydrostatic pressure may change the DPG volume and compress any gas entrained in the mineral oil at sea level. The Lacoste-Romberg gravimeter is sensitive to zero-frequency temperature changes because the viscosity of the gas in the gravimeter beam damper decreases with a temperature decrease (approximately a 4% decrease from 25°C to 0°C), the elastic constant of the instrument spring changes, and the electrolytic level indicators may be offset. The decrease in viscosity can change a critically damped system to an underdamped (resonant) one, but the 4% viscosity change is small enough that it probably has little effect. Changes to the gravimeter spring constant can change a critically damped system to an underdamped or overdamped one. Finally, the frequency response of the gravimeter beam

is sensitive to temperature-induced changes in the gravimeter long level.

DPGs are calibrated on the seafloor by activating a solenoid that lifts one gauge 1.00 cm, creating an easily computed decrease in hydrostatic pressure. One DPG is lifted at a time, and the response of the pressure card voltage to the pressure step gives both a zero-frequency gain value and the time constant of the capillary leak. The calibration is masked by microseism energy, but the microseism energy measured on the second differential gauge can be subtracted from the gauge being calibrated. To double check the calibrations, the transfer function between the two DPGs is calculated from ambient seafloor pressure data.

The zero-frequency gain of the gravimeter is determined by moving the micrometer screw and noting the correlation between micrometer screw turns and beam position voltage. Each micrometer screw turn corresponds to a known change in acceleration supplied in a table provided with the gravimeter. To determine the ADOCS gravimeter's low temperature frequency response, we deployed the tethered and heated Lacoste-Romberg gravimeter next to the ADOCS for a three-hour acceleration measurement during a deep-ocean experiment. The data allowed a transfer function between the two instruments to be calculated. Later, the heated Lacoste-Romberg gravimeter was tested alongside a calibrated IDA network Lacoste-Romberg gravimeter to verify that the heated instrument's frequency response is flat over the frequency range of interest.

5.6 Conclusions

The autonomous compliance sensor provides superior compliance measurements to those obtained by the tethered gravimeter with a lowered demand on ship time. The instrument is not heated, but instead equilibrates with ambient seafloor temperature to save power and to extend compliance measurements' low frequency range. The temperature effect on the gravimeter is important, and necessitates confirmation of the instrument gain on the seafloor through micrometer screw calibration and comparison of acceleration spectra with a heated instrument.

Chapter 6

Juan de Fuca Ridge Shear Velocity Profiles

6.1 Introduction

The Juan de Fuca Ridge is a medium spreading rate (6 cm/yr) spreading center situated 200-500 km off the northwest coast of the United States. Because of its proximity, the ridge has been extensively studied, including dense bathymetric mapping, submersible dives, drilling, side-scan sonar, deep towed experiments, surface and seafloor gravity experiments, and active seismic experiments. None of the numerous seismic experiments on the Juan de Fuca Ridge have unambiguously located an axial magma chamber, although two seismic reflection surveys [*Morton et al.*, 1987; *White and Clowes*, 1990] detected a faint reflector underneath the ridge crest, and a seismic reflection study [*Christeson et al.*, 1993] includes a magma cham-

Figure 6.1: SEABEAM bathymetry of the Juan de Fuca Ridge from 44°40'N to 48°20'N. Compliance sites are shown as circles.

ber model as one of three possible models that fit their data. Low shear velocity is associated with the presence of partial melt [*Schmeling, 1985*], but — as is the case with most seafloor sites — the Juan de Fuca Ridge shear velocity structure is poorly constrained. Seafloor compliance inversion provides a method to look for crustal regions of low shear velocity [*Crawford et al., 1991*].

In August and September 1993, during two legs of the REM expedition aboard the R/V *Melville*, we deployed an autonomous compliance sensor to measure seafloor acceleration and pressure on four young (less than 80 Ka) near-axis sites on the Juan de Fuca Ridge (figure 6.1). The instrument consists of a Lacoste-Romberg gravimeter [*Lacoste et al., 1967*] used as a long-period seismometer and two differential pressure gauges [*Cox et al., 1984*]. Seafloor pressure and acceleration spectra are used to calculate seafloor compliance [*Crawford et al., 1991*], which is inverted to determine the seafloor shear velocity structure to 5000 mbsf. Recently, data from a Department of Defense array of seafloor hydrophones (SOSUS) has allowed sensing of seismic/volcanic events on the ridge [*Fox et al., 1993*]. Two compliance measurements were made near the June-July 1993 path of magma upwelling and lateral injection recorded by the SOSUS array.

6.2 Measurement and Data Analysis

This experiment marks the first autonomous deployments of the Lacoste-Romberg gravimeter; previous compliance measurements [*Crawford et al.*, 1991] were made using a tethered instrument. The instrument was deployed for 2-3 days at each site. To allow time for thermal equilibration, data are analyzed from the second day forward. The long period seismometer is sensitive to temperature variations but no heater is used in the current design for battery power considerations. Instead, the instrument equilibrates with the ambient seafloor temperature during the first day of each deployment. Data are sampled at a rate of 2 Hz and saved on an onboard hard disk. The long-period seismometer and two differential pressure gauges occupy three data channels. A fourth data channel contains multiplexed data used to determine instrument status and to locate data errors.

Pressure and acceleration data are examined to remove bad sections. The data are prewhitened (filtered) using a 4-pole bandpass (0.002 to 0.035 Hz) filter to reduce contamination at low frequencies by energy in the microseism peak through broadband spectral leakage. Figure 6.2 shows the dominance of energy in the microseism (0.08–1 Hz) and thermal noise (0.001–0.004 Hz) frequency bands over seafloor acceleration energy in the infragravity wave band (0.004–0.02 Hz). Prewhitening allows use of a 1π prolate spheroidal data window with a narrow passband but moderate (50 dB) broadband signal rejection. Cross-spectra are calculated using a 2048-point 1π prolate spheroidal window. The angular distribution of the cross-spectra is calculated in order to eliminate cross-spectra that significantly deviate

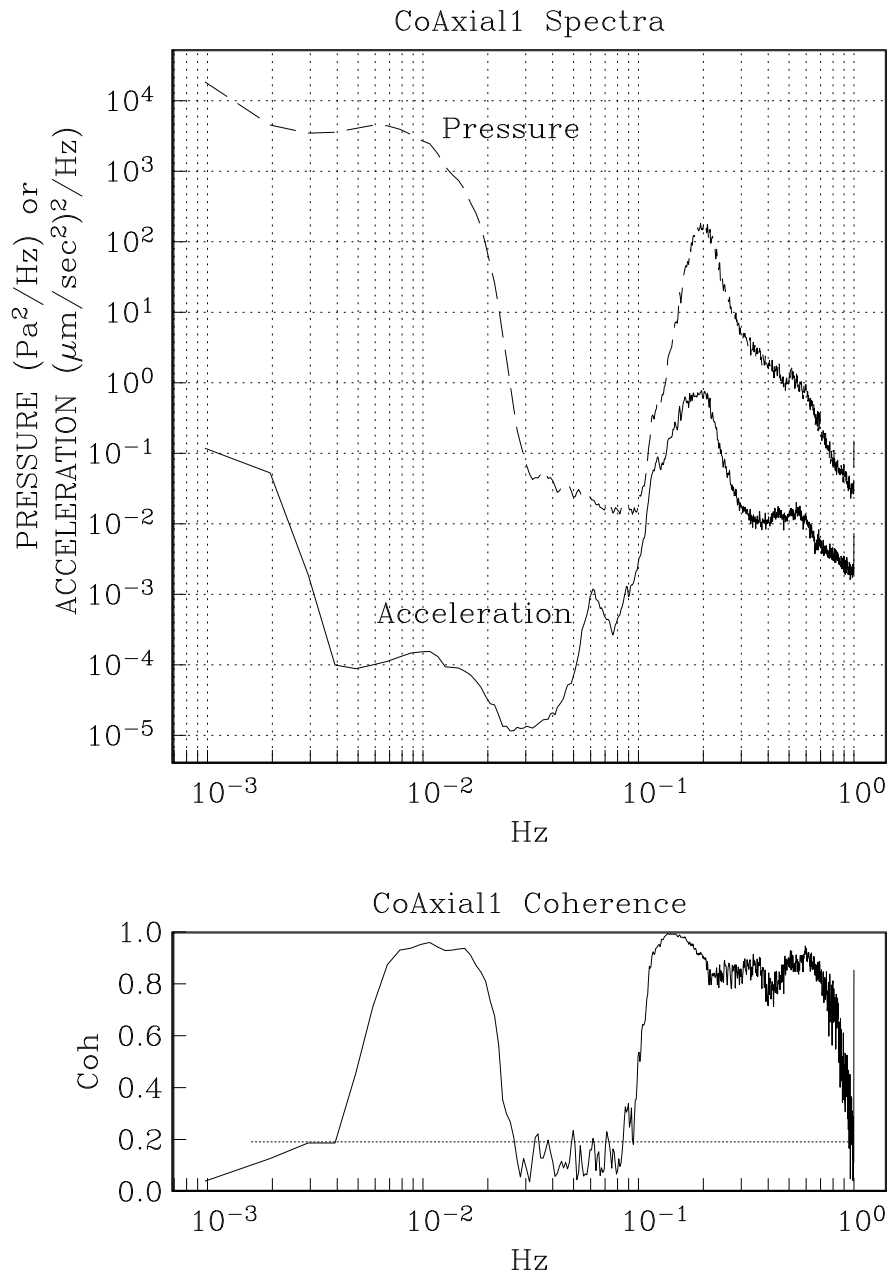


Figure 6.2: Spectra and coherence calculated from site COAXIAL1 on the southern Coaxial segment, Juan de Fuca Ridge. A 4π prolate spheroidal window was applied to the data before calculating the Fourier transform. A 1π window is used when calculating compliance. The 1π window has better narrow-band signal isolation but requires prefiltering which alters the shape of the spectra.

from the distribution. This technique borrows from the method of robust coherence [Chave *et al.*, 1987], which weights spectra according to their position in a distribution of cross-spectra. We reject rather than down-weight data windows because we believe that the cross-spectra that fall far outside the calculated distribution are due to discrete events such as small earthquakes that invalidate the data window. Finally, accepted windows are used to calculate acceleration compliance (equation 3.3), which is converted to normalized compliance by multiplying by k/ω^2 .

Seafloor pressure and acceleration data were collected at four sites on the Juan de Fuca Ridge (figure 6.1). Data were collected for 47 hours at site CLEFT1, located in the axial valley of the Cleft segment at $44^{\circ}39.708'N$, $130^{\circ}21.984'W$. Data collection lasted 47 and 62 hours at sites COAXIAL1 and COAXIAL2 on the Juan de Fuca Ridge's Coaxial segment. Site COAXIAL1 is near the south of the segment at $46^{\circ}13.584'N$ $129^{\circ}43.853'W$, while site COAXIAL2 is 30 km further north at $46^{\circ}28.446'N$ $129^{\circ}36.815'W$. Data were collected for 66 hours at site ENDEAV1, located approximately 4 km (0.07 Ma) off of the Endeavour segment axis, at $47^{\circ}56.474'N$ $129^{\circ}02.844'W$.

Compliance inversion requires approximate compressional velocity and density models to construct a shear velocity model. Compressional velocity and density models are constructed from gravity [Stevenson *et al.*, 1994] and active seismic surveys near the sites. The upper 1200 meters of the compressional velocity model used for site CLEFT1 is from a seismic refraction study of the northern Cleft segment and the Cleft-Vance overlapper by McDonald *et al.* [1994]. For sites COAXIAL1

and COAXIAL2, we use a compressional velocity model from a seismic refraction study of the Coaxial segment from 46°40' to 47°04'N by *Christeson et al.* [1993]. The ENDEAV1 compressional velocity model is from *Cudrak and Clowes* [1993]. Deep structure at sites CLEFT1 and ENDEAV1 is based on *Christeson et al.* [1993] and *Spudich and Orcutt* [1980]. Shear velocities for the starting models are calculated by dividing the compressional velocity by 1.87. Where experimental densities are not available, we use the following relation between seismic compressional velocity (V_P , km/s) and density (ρ , g/cc) [*Carlson and Raskin*, 1984]:

$$V_P < 6.65 \text{ km/s} : \rho = 3.50 - 3.79/V_P, \quad (6.1)$$

$$V_P \geq 6.65 \text{ km/s} : \rho = 3.81 - 5.99/V_P.$$

6.3 Inversion

Figure 6.3 shows compliances estimated at the four sites. Above 0.013 Hz, CLEFT1 and COAXIAL1 compliances are similar, while the Endeavour site is significantly more compliant. Between 0.005 and 0.013 Hz, there is a region of high compliance in the CLEFT1 data, suggesting low shear velocities at depth. The compliance datum from site COAXIAL2 is much higher than any of the other compliances.

One-dimensional shear velocity (V_S) structure beneath the experiment sites is estimated using a linearized inversion method called Occam's inversion [*Constable et al.*, 1987]. The inversion method minimizes the second derivative (curvature) of the V_S model, fitting minimum model structure to the data. The compliance

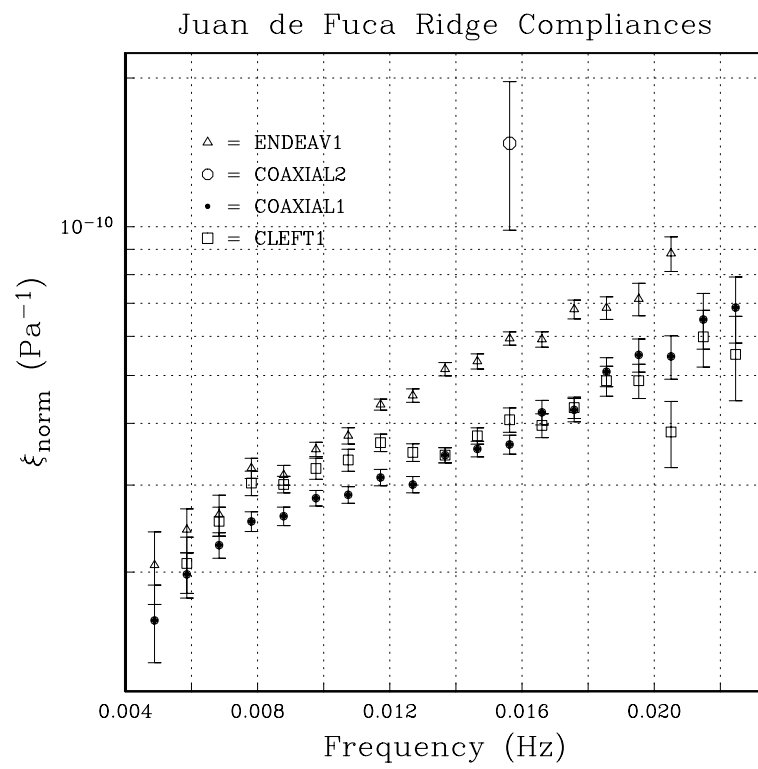


Figure 6.3: Seafloor compliances measured at four sites on the Juan de Fuca Ridge.

function has a significant dependence on shear velocity at depths approximately $1/6$ the wavelength λ of the forcing waves. The linear surface gravity waves obey a dispersion relation $\omega^2 = gk \tanh(kH)$, where g is gravitational acceleration, $k = 2\pi/\lambda$ is the wavenumber, and H is the water depth. At CLEFT1, $H = 2222$ meters, and the smallest useful compliance frequency (f_{min}) is 0.0047 Hz, so that the measured compliance is influenced by structure at a maximum depth (d_{max}) of 5.0 km. The d_{max} at site COAXIAL1 ($H = 2183$ m, $f_{min} = .0047$ Hz) is comparable. At site ENDEAV1 ($H = 2364$ m, $f_{min} = .0047$ Hz) d_{max} is slightly deeper (5.2 km). Site COAXIAL2 could not be inverted for shear velocity structure because there was only one useful compliance datum.

V_S profiles at sites CLEFT1, COAXIAL1, and ENDEAV1 (figure 6.4) are determined by inversion of compliance data (figure 6.3) using approximate V_P models (figure 6.5). Compliance from site COAXIAL2 is not inverted because there is only one datum. The CLEFT1 shear velocity profile contains a region of low shear velocity at a depth of 1500-5000 meters. ENDEAV1 shear velocities are generally lower than shear velocities at the other two sites. Site COAXIAL1 has a comparatively smooth shear velocity structure, except near the surface where the data require relatively low shear velocities.

6.3.1 Cleft segment

The Cleft segment is the southernmost segment of the Juan de Fuca Ridge, extending from $44^\circ 27'$ to $45^\circ 05'N$. Cleft segment is often descriptively divided into

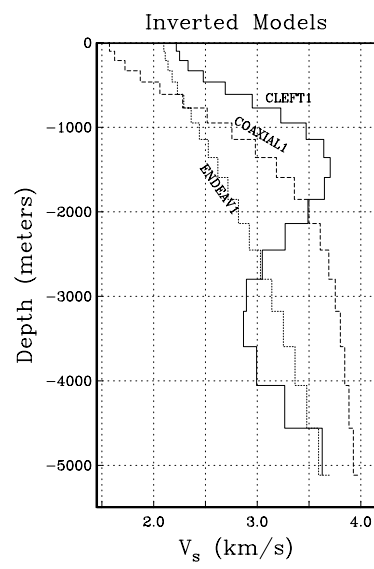


Figure 6.4: Shear velocity models determined by inversion of compliances.

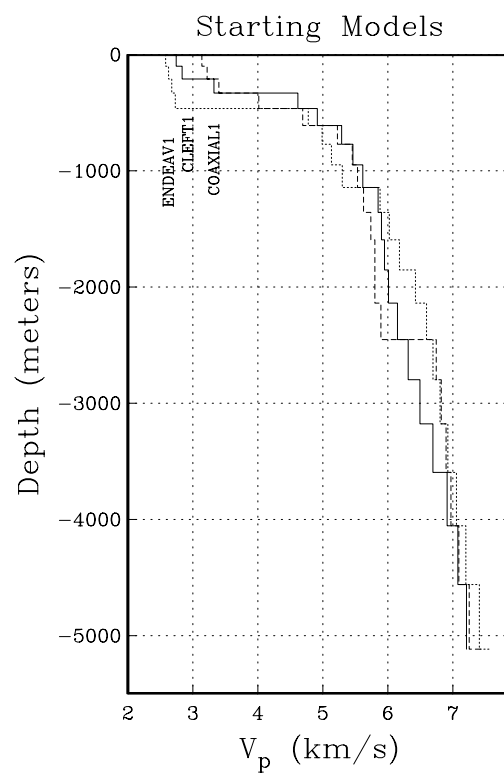


Figure 6.5: Compressional velocity models used during compliance inversion. Primary sources of compressional velocity data are *McDonald et al.* [1994] for the Cleft segment, *Christeson et al.* [1993] for the Coaxial segment, and *Cudrak and Clowes* [1993] for the Endeavour segment.

north and south segments, which *Embley et al.* [1991] suggest are fed by separate crustal magmatic reservoirs. The northern Cleft segment (latitudes above $44^{\circ}44'N$) has recently undergone a spreading episode, evidenced by large hydrothermal plumes, fresh glassy basalts, and a constructional volcanic mound that appeared in the last ten years [*Fox et al.*, 1992]. We measured compliance on the south Cleft segment, less than 200 meters from the 10 m deep by 20-30 m wide cleft that runs along axis from $44^{\circ}35'$ to $44^{\circ}44'N$ and gives the segment its name. The neovolcanic zone of the south Cleft segment is estimated to be less than a few hundred years old [*Normark et al.*, 1983]. *Morton et al.* [1987] detected a ridge-axis reflector which they interpret as the top of a magma chamber 2300-2500 mbsf on their line 102, which crosses site CLEFT1.

Inversion of CLEFT1 compliance reveals a region of low shear velocity between 1500 and 5000 mbsf, with the shear velocity minimum 3200 mbsf. The shear velocity model suggests a magma chamber beneath the CLEFT1 site. The most widely accepted axial magma chamber model consists of a thin, narrow melt lens (10–1000 m high by less than 3 km wide) melt lens overlying a zone of crystal mush [*Sinton and Detrick*, 1992; *Kent et al.*, 1993], with possibly a several hundred meter thick transition from melt to crystalline mush [*Detrick and Toomey*, 1992]

To constrain the depth and vertical extent of the CLEFT1 site magma chamber, we compare measured compliance to compliances calculated from various magma chamber models. Two groups of magma chamber models are considered: the first group contains only a discrete low velocity layer (the region of partial melt), and

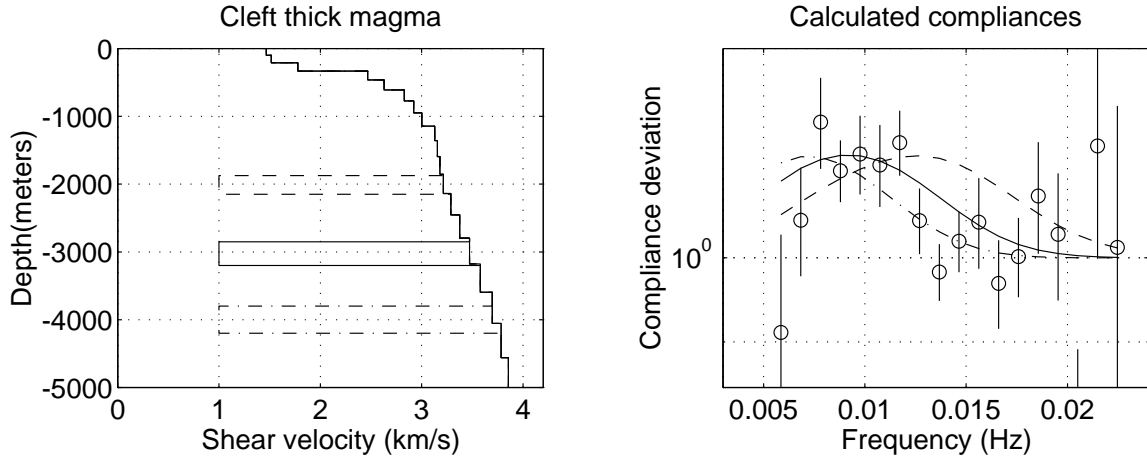


Figure 6.6: Models and resulting compliances for an approximately 300 meter thick discrete layer of magma underlying the Cleft compliance site. Compliances are normalized by dividing by compliance of the *McDonald et al.* [1994] model.

the second group adds a zone of reduced shear velocity (the crystal mush region) beneath the melt lens. Figure 6.6 shows models with a 300 meter thick magma chamber superposed on the *McDonald et al.* [1994] model, and compliances calculated from these models compared with the CLEFT1 compliance data. All compliance data are normalized by dividing by the compliance of the *McDonald et al.* [1994] model. Figure 6.7 calculates compliances of the *McDonald et al.* [1994] model with a thin (20 meter thick) magma lens superposed. The computational assumption of infinite lateral extent for all features de-emphasizes the shear velocities of features with limited lateral extent (such as magma chambers). Assuming a thick (300 m) magma layer ($V_S = 1$ km/s, figure 6.6) the best fit to the data is a magma chamber centered at 3000 m or slightly higher. Modeling the magma layer as 20 m thick (figure 6.7)

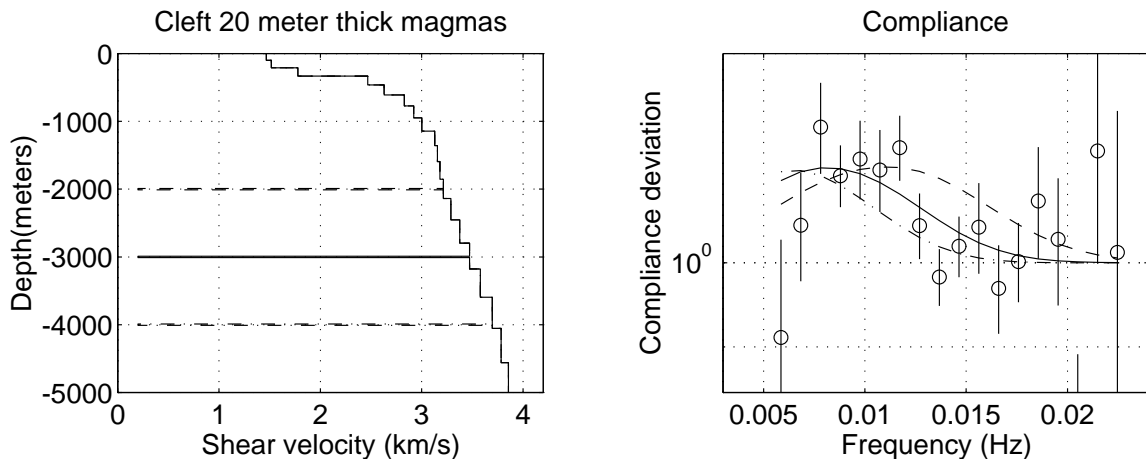


Figure 6.7: Models and resulting compliances for a 20 meter thick discrete layer of magma underlying the Cleft compliance site. Compliances are normalized by dividing by compliance of the *McDonald et al.* [1994] model.

requires a significant decrease in shear velocity within the low velocity layer (to 0.2 km/s), which shifts compliances to lower frequencies. The best fit for a thin magma chamber is 2500 ± 200 meters deep. The shape of the high compliance peak for the 300 m thick low velocity layer models is almost indistinguishable from shape of the compliance peak calculated from a 20 m thick low velocity layer. The compliance peak calculated from a very thin low shear velocity layer is approximately 0.008 Hz, while the frequency-depth relationship for compliance (figure 6.8) reveals that the frequency band from 0.008 to 0.012 Hz (half of the “impulse response” bandwidth, centered at the location of the CLEFT1 compliance peak) covers about 1000 meters of structure. Therefore we are unable to resolve the difference between a 20 m thick magma layer and a 1000 m thick magma layer.

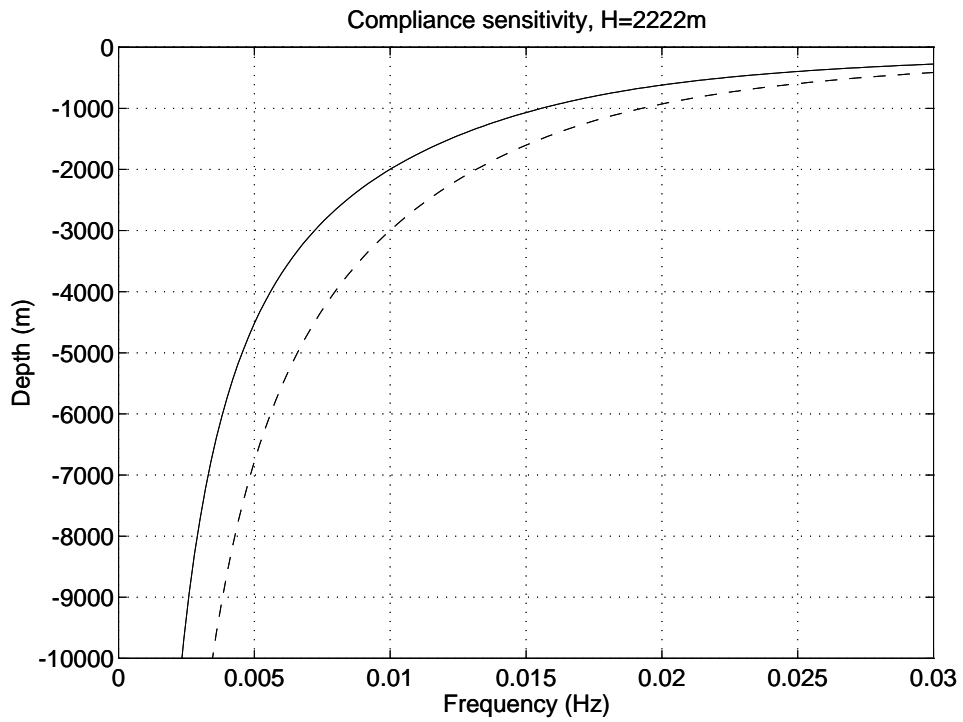


Figure 6.8: Relationship between compliance frequency and depth of greatest sensitivity. Dashed line is calculated using a slight decrease in shear velocity, and represents the frequency-depth relationship for small structures in compliance data. Solid line is calculated using a nearly zero shear velocity zone, and is more accurate for features with very low shear velocity.

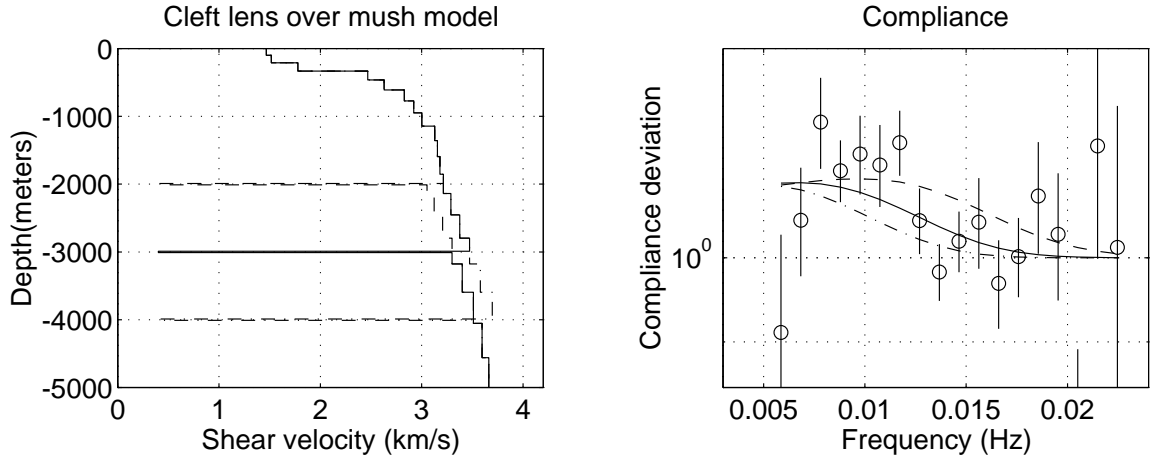


Figure 6.9: Models and resulting compliances for a 20 meter thick discrete layer of magma overlying partially molten crystal mush. Compliances are normalized by dividing by compliance of the *McDonald et al.* [1994] model.

Sinton and Detrick [1992] model a region of crystal mush underlying a mid-ocean ridge melt lens, and *Vera et al.* [1990] detected reduced compressional velocities beneath the magma lens on the East Pacific Rise axis (V_P approximately 15% below values found off-axis). Figure 6.9 shows models and compliances of site CLEFT1 with a region of crystal mush underlying the melt lens. The crystal mush region is modeled by diminishing starting model seismic velocities by 5% below the magma region, but this small change broadens the modeled compliance peak beyond the range of the compliance data. This result suggests the site CLEFT1 magma chamber does not overly a thick layer of crystal mush. Instead, magma probably arrived at the site through lateral injection from another upwelling location, or as a discrete lens that rose from the mantle through solid crustal rock.

The compliance data are interpreted as representing a magma chamber located 2000–2500 mbsf (for a thin layer) and 2800–3300 mbsf (for a thick layer). If we accept the *Kent et al.* [1990, 1993] model of a melt lens only 10-50 m thick, the top of the magma chamber is located 2000–2500 mbsf. The magma chamber is discrete and does not grade into an extensive region of crystal mush below.

The depth of the Cleft segment magma chamber fits a trend of increasing magma chamber depth with decreasing spreading rate noted by *Purdy et al.* [1992]. The trend is based on six magma chamber determinations from slow, medium, and fast spreading centers. *Purdy et al.* [1992] suggest that magma chambers are deeper at slower spreading ridges because they are more deeply faulted, resulting in hydrothermal circulation (and therefore cooling) to greater depths. The magma chamber detected at site CLEFT1 (2000-2500 mbsf, 6cm/yr spreading rate) is shallower than magma chambers detected at the slow-spreading Mid-Atlantic Ridge (3000-4000 mbsf, 2.5 cm/yr spreading rate) and deeper than those on the fast spreading East Pacific Rise (1000-2000 mbsf, 11-15 cm/yr spreading rate). *Purdy et al.* [1992] also noted two sites with spreading rates comparable to the Cleft segment: Lau Basin and the Coaxial segment of the Juan de Fuca Ridge. The Cleft magma chamber is shallower than either of these, although it should be noted that the Coaxial segment magma chamber model [*Christeson et al.*, 1993] was one of three models presented that fit the data equally well.

6.3.2 Coaxial segment

Figure 6.10 shows the Coaxial segment of the Juan de Fuca Ridge (also known as the Cobb segment or the Northern Symmetrical segment). The seafloor instrument was deployed at two locations on the Coaxial segment. The first site, three km east of the middle of the Coaxial valley, is at approximately the same latitude as a proposed site of magma upwelling on 26 June 1993 that initiated a lateral dike injection north-northeast along the ridge until the magma reached the surface just north of a small volcano at $46^{\circ}32'N$ $129^{\circ}34'W$ [Fox *et al.*, 1993]. The U.S. Navy's SOSUS array of hydrophones located the upwelling site and southern end of the subsequent dike within the north flank of Axial Volcano, but subsequent on-site surveys detected active hydrothermal vents and bacterial floc sites in the middle of Coaxial valley, suggesting that upwelling actually occurred in the center of Coaxial valley and that the seismic T-phases detected by the SOSUS array were topographically steered away from the event epicenters. The second deployment site was 30 km north-northeast of site COAXIAL1, lying directly on top of the proposed dike 5 kilometers south of fresh lava flows believed to have erupted from the dike. The COAXIAL1 deployment was approximately 60 days after the start of the swarm, and the COAXIAL2 deployment took place 30 days later.

COAXIAL1 compliance resembles CLEFT1 compliance, but the compliance is flat enough that the estimated V_S profile does not contain a region of low shear velocity. The inversion minimizes shear velocity model structure, so the results do not rule out the presence of an axial magma chamber, but comparison of the COAXIAL1

Coaxial segment

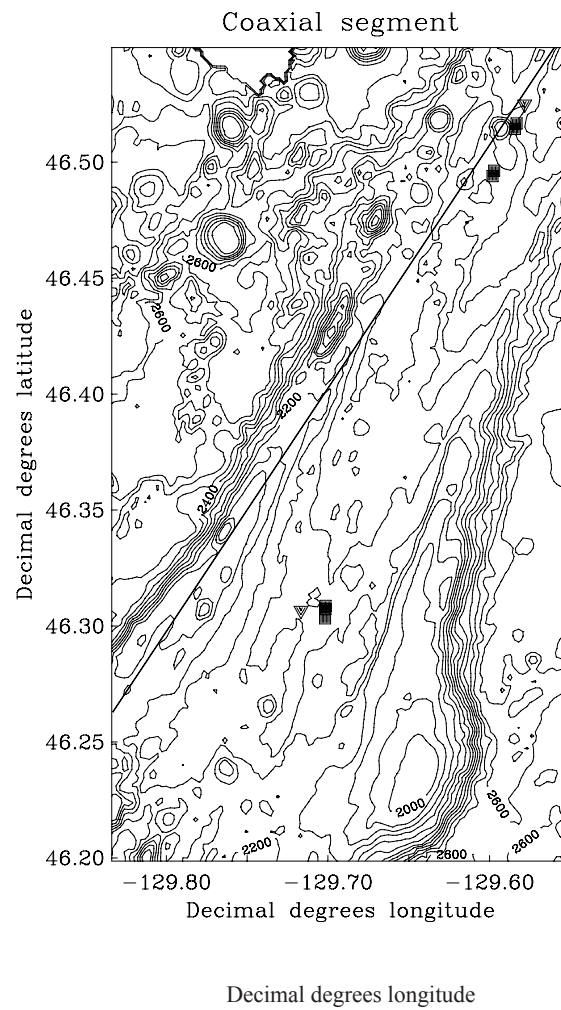


Figure 6.10: Coaxial segment of the Juan de Fuca Ridge. Thick line is the linear best fit to SOSUS array epicenter determination of the June-July 1993 seismic swarms. Squares and triangles indicate hydrothermal vents, fresh lava flows, and bacterial floc sites observed following the swarm onset. Circles are seafloor compliance measurement sites.

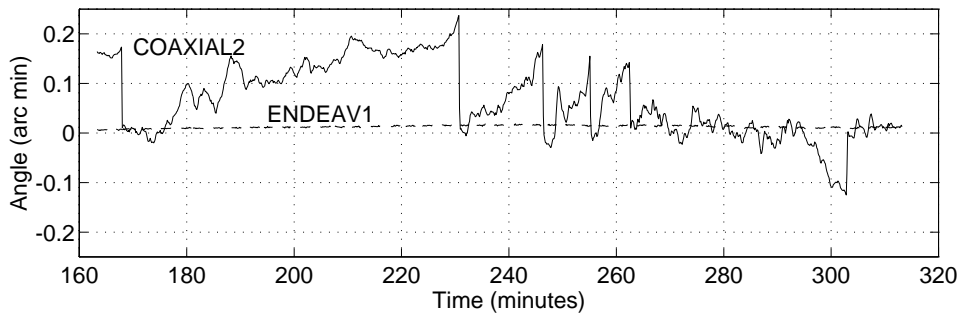


Figure 6.11: Deviation of instrument from horizontal level at a typical compliance site (ENDEAV1) and at site COAXIAL2 which overlies a magma injection dike on the Coaxial segment of the Juan de Fuca ridge. Sudden jumps of level to near 0 reflect instrument releveing.

site compliance with the CLEFT1 site compliance suggests any magma chamber at COAXIAL1 is much smaller than at CLEFT1.

At site COAXIAL2, the gravimeter levels (figure 6.11) fluctuated throughout the deployment, possibly due to harmonic tremor, hydrothermal activity, or microearthquakes. There was just enough quiescent data to calculate compliance in one frequency bin, at 0.155 Hz. Compliance measured at 0.0155 Hz at site COAXIAL2 (figure 6.3) is 3 times greater than compliance at CLEFT1 or COAXIAL1. The high compliance at this frequency is consistent with low shear velocity within the upper 2000 m of the crust. In section 6.3.3, high ENDEAV1 compliance is shown to be the result of thick layer 2A, but the one compliance datum from site COAXIAL2 is much higher than compliance from site ENDEAV1, suggesting that shear velocities are significantly lower. The high compliance is probably the result of shallow magma.

Although sites COAXIAL1 and COAXIAL2 are both near the center of

the Coaxial valley, only the northern site shows any evidence of low shear velocity within the crust. The southern site is approximately 3 km laterally away from one postulated location of recent magma upwelling. Compliance inversion at that site averages structure over at least 5 km at the deepest model depths, so the compliance data should see some indication of the proposed upwelling site. Since there is no indication of low shear velocity 5 km beneath the center of Coaxial valley, we conclude that the site of magma upwelling is within the north rift zone of Axial volcano, as determined by the SOSUS array of hydrophones [Fox *et al.*, 1993], and that the hydrothermal vents and bacterial flocs discovered in the center of Coaxial valley are not related to that event.

6.3.3 Endeavour segment

Site ENDEAV1 is approximately 4 km (70,000 years) off of the axis of the Endeavour segment of the Juan de Fuca Ridge. The site is located off-axis because the instrument failed to level during two earlier on-axis deployments, and a sidescan sonar map indicated that this site was relatively smooth. The site is located approximately 1 km south of coincident seismic reflection and refraction lines [Rohr *et al.*, 1988; White and Clowes, 1990], and is near the center of a 3-D tomographic compressional velocity experiment [Cudrak and Clowes, 1993]. The Endeavour segment displays no recent volcanism and appears to have developed a summit depression, both of which indicate a state of diminished magma supply with a very small or no magma chamber. Cudrak and Clowes [1993] determined that layer

2A is much thicker on the Endeavour segment (400 ± 200 m) than has been observed at several other sites elsewhere on the Juan de Fuca Ridge. Thickness of seismic layer 2A is suggested to be a function of the ratio of pillow lavas to sheet flows in the extrusive volcanic region [Bonatti and Harrison, 1988]. A high ratio of pillow lavas to sheet flows would result in lower velocities due to the voids between pillows. Furthermore, Bonatti and Harrison [1988] suggest that the ratio of pillows to sheet flows depends on spreading rate, because slower spreading rate ridges have cooler, more viscous lavas.

Compliance inversion of the ENDEAV1 data results in significantly lower shear velocities than at the other sites at almost all depths (figure 6.4). However, the compliance data can be fit by a very thick (approximately 700 m thick) layer 2A. The inverted model is maximally smooth and so uncertainty in compliance data allows low shear velocities determined by compliance inversion to extend below the bottom of a low shear velocity layer (see, for example, figure 3.7). The shape of the compliance curve precludes a deep low velocity layer associated with a magma chamber. Figure 6.12 shows different models of layer 2A thickness and resulting compliances calculated from these models. Of the three layer 2A thickness models (450 m, 750 m and 1500 m), a 750 m thick layer 2A fits the data best.

To better constrain layer 2A thickness, we invert compliance data to determine shear velocities with the structure-minimizing constraint removed at one (predefined) layer interface, allowing a jump in V_S at the interface. Compressional velocity models were constructed assuming layer 2A thicknesses of 450, 610, 770

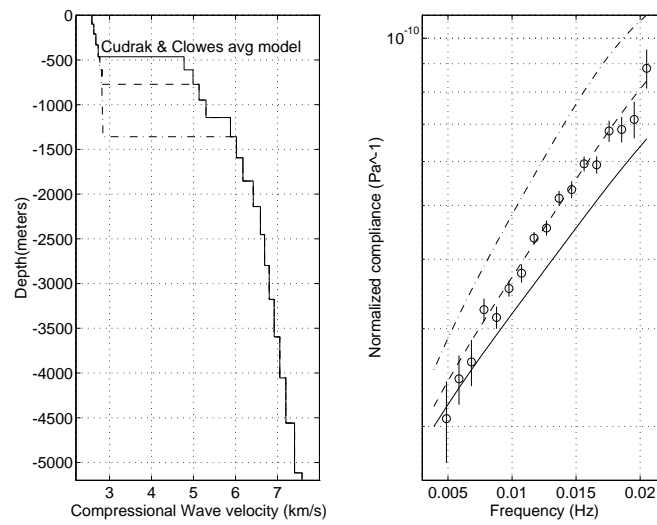


Figure 6.12: Models and resulting compliances for different layer 2A thicknesses at the Endeavour site: a) compressional velocity models (solid line = *Cudrak and Clowes* [1993] model, b) resulting transfer functions superposed on the Endeavour site transfer function.

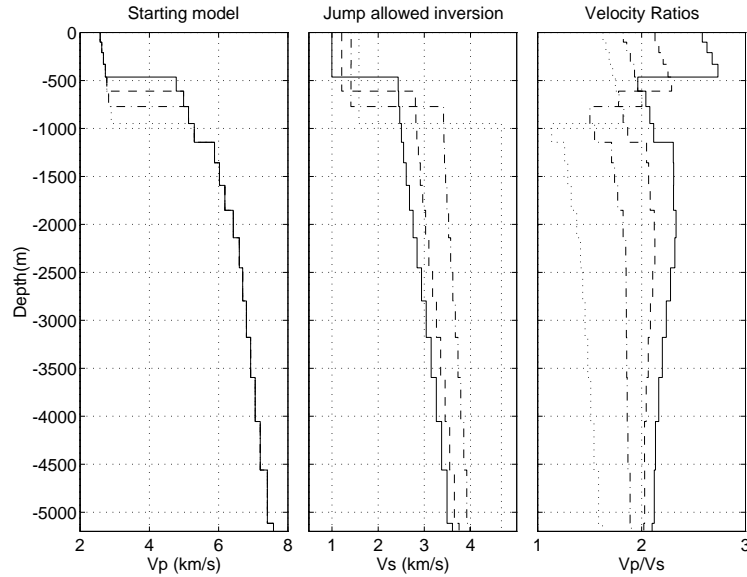


Figure 6.13: Starting models and resulting V_S inversions allowing a jump at the 2A/2B interface for different layer 2A thicknesses at the Endeavour site: a) compressional velocity models (solid line = *Cudrak and Clowes* [1993] model, b) resulting V_S models, c) V_P/V_S ratios for the models of figures A and B.

and 950 m, and the data were inverted for shear velocities with a jump allowed in the shear velocity model at the same depth as the corresponding jump in the compressional velocity model. Figure 6.13 shows compressional velocity models, shear velocity models obtained by compliance inversion, and V_P/V_S for each of the models. Since *Cudrak and Clowes'* layer 2A velocity gradient is poorly constrained, and the inversion minimizes model structure and not V_P/V_S structure, the shape of the V_P/V_S model is not well constrained, but the values should fall somewhere in the range 1.8-2.4 [*Spudich and Orcutt*, 1980]. Only the 610 m and 770 m layer 2A models are in this range.

Another method of determining layer 2A thickness is to invert for both V_S

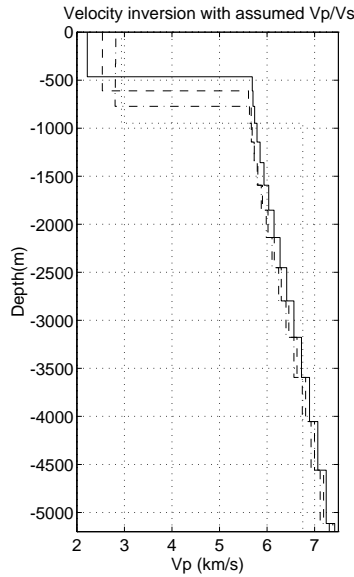


Figure 6.14: Inversions of different 2A layer thickness models, with $V_P/V_S = 1.85$ below layer 2A and increasing linearly to $V_P/V_S = 2.32$ at the seafloor.

and V_P by assuming a model of V_P/V_S throughout the crust. This technique is not used for determining V_S because there is no reason to believe that V_P/V_S is well known in young oceanic crust, but it provides a somewhat independent method of estimating layer 2A thickness. The resulting crustal models with V_P in layer 2A closest to the layer 2A velocity of 2.56–2.66 km/s [Cudrak and Clowes, 1993] is the closest model to the actual layer 2A thickness. V_P/V_S models for 450, 610, 770, and 950 m thick layer 2A were constructed using $V_P/V_S = 2.32$ at the surface [Vera *et al.*, 1990] and decreasing to 1.85 at the layer 2A/2B interface, below which V_P/V_S is constant at 1.85. Figure 6.14 shows inversion results for the same starting models as in figure 6.13. V_P in layer 2A is highly dependent on layer 2A thickness. The 610-meter-thick layer 2A model has $V_P = 2.5$ km/s and the 770-meter-thick layer

2A model has $V_P = 2.8$ km/s. The best fit to the *Cudrak and Clowes* compressional velocities is somewhere between these two models, suggesting layer 2A thickness of 700 ± 50 m.

The layer 2A thickness determined is at the upper bound of layer 2A thicknesses estimated by *Cudrak and Clowes*. The authors had well-defined travel times through layer 2A; we believe ENDEAV1 is situated on locally thick layer 2A. Seafloor compliance measurements reflect lateral structure over a horizontal range of somewhere between the depth sensitivity of compliance inversion and the wavelength of the forcing waves. We expect that the 700 m thick layer 2A we find is averaged over a 700 to 4000 m horizontal range.

Thick layer 2A at the Endeavour segment may be the result of a high ratio of pillow lavas to sheet flows in the extrusive volcanic layer. *Bonatti and Harrison* [1988] found that the ratio of pillows to massive units is a function of spreading rate, with a larger relative percentage of pillows produced on crust at slower spreading ridges. The Endeavour segment, while not considered a slower spreading ridge, appears to be much less active than the Cleft, Vance, and Coaxial segments. The sediment cover on the axial valley lava flows dates them at approximately 10,000 yr [*Davis et al.*, 1984], compared to zero-age to 2,000 yr lavas on the other segments [*Normark et al.*, 1982; *Fox et al.*, 1992]. The very thick layer 2A may be the result of a high relative percentage of pillow formation due to low temperature/high viscosity magma supplied to the surface from a depleted magma chamber.

6.4 Conclusions

1. There is a region of low shear velocity beneath the Cleft segment ridge axis at $44^{\circ}39.7'N$. This low velocity zone probably corresponds to an axial magma chamber. Assuming a discrete and thin (less than 100 m thick) region of partial melt, the magma chamber is centered between 2000 and 2500 mbsf. The data indicate there is no extended region of crystal mush beneath the magma chamber, suggesting that the magma arrived at the site through lateral injection or as a discrete lens that rose through solid rock to a level of density equilibrium.
2. There is no evidence for an axial magma chamber at site COAXIAL1 on the southern Coaxial segment of the Juan de Fuca Ridge, 3 km from the ridge axis. Farther north, and directly on top of a linear zone of earthquakes, site COAXIAL2 has very high compliance at 0.0155 Hz, consistent with low shear velocities within the upper 2000 meters of the crust. The data support SOSUS array epicenter determinations of magma upwelling and dike propagation starting at the north flank of Axial Volcano and traveling north-northeast to the middle of Coaxial segment valley 30 km to the north in late July 1993. Hydrothermal vents and bacterial flocs discovered in the middle of the valley by on-site surveys soon after the start of the swarm are probably not related to the upwelling and dike propagation event.
3. The Endeavour segment layer 2A averages 700 m thickness over at least one

kilometer surrounding the compliance measurement site. This is at the high extreme of layer 2A thickness determined by *Cudrak and Clowes* [1993] at this site, and supports their evidence of relatively thick layer 2A on the Endeavour segment. Thick layer 2A may be the result of a high ratio of pillow lavas to massive flows, caused by low temperature and high viscosity of magma beneath the depleted Endeavour segment. There is no evidence for a crustal magma chamber beneath the experiment site (four km off axis).

Bibliography

- [1] E. Bonatti and C.G.A. Harrison. Eruption styles of basalt in oceanic spreading ridges and seamounts: effect of magma temperature and viscosity. *J. of Geophys. Res.*, 93:2967–2980, 1988.
- [2] R.L. Carlson and G.S. Raskin. Density of the oceanic crust. *Nature*, 311:555–558, 1984.
- [3] A.D. Chave, D.T. Thomson, and M.E. Ander. On the robust estimation of power spectra, coherences, and transfer functions. *J. of Geophys. Res.*, 92:633–648, 1987.
- [4] G.L. Christeson, G.M. Purdy, and G.J. Fryer. Structure of young crust at the East Pacific Rise near 9°30'N. *Geophys. Res. Let.*, 19:1045–1048, 1992.
- [5] G.L. Christeson, G.M. Purdy, and K.M.M. Rohr. Structure of the northern symmetrical segment of the Juan de Fuca Ridge. *Marine Geophys. Res.*, 15:219–240, 1993.
- [6] S.C. Constable, R.L. Parker, and C.G. Constable. Occam's inversion: a practical algorithm for generating smooth models from electromagnetic sounding data. *Geophys.*, 52:289–300, 1987.
- [7] C.S. Cox, T. Deaton, and S. Webb. A deep-sea differential pressure gauge. *J. of Atmos. and Oceanic Tech.*, 1(3):237–246, 1984.
- [8] W.C. Crawford, S.C. Webb, and J.A. Hildebrand. Seafloor compliance observed by long-period pressure and displacement measurements. *J. of Geophys. Res.*, 96:16151–16160, 1991.

- [9] C.F. Cudrak and R.M. Clowes. Crustal structure of Endeavour ridge segment, Juan de Fuca Ridge, from a detailed seismic refraction survey. *J. of Geophys. Res.*, 98:6329–6349, 1993.
- [10] E.E. Davis, R.G. Currie, R.P. Riddihough, W.B.F. Ryan, K. Kastens, D.M. Hussong, S.R. Hammond, and A. Malahoff. Geological mapping of the northern Juan de Fuca and Explorer Ridges using SeaMARC I, SeaMARC II, and Seabeam acoustic imaging. *EOS, Trans. Am. Geophys. Un.*, 65:1110, 1984.
- [11] R.S. Detrick, P. Buhl, E. Vera, J. Mutter, J. Orcutt, J. Madsen, and T. Brocher. Multi-channel seismic imaging of a crustal magma chamber along the East Pacific Rise. *Nature*, 326:35–41, 1987.
- [12] R.S. Detrick and D.R. Toomey. Geophysical constraints on mid-ocean ridge magma chambers and crustal structure. Lecture notes from the Ridge Theoretical Institute Short Course on Hydrothermal and Magma Chamber Processes at Mid-Ocean Ridges, 1992.
- [13] R.W. Embley, W. Chadwick, M.R. Perfit, and E.T. Baker. Geology of the northern Cleft segment, Juan de Fuca Ridge: recent lava flows, sea-floor spreading, and the formation of megaplumes. *Geology*, 19:771–775, 1991.
- [14] C.G. Fox. Detection and response to a seafloor spreading event. *RIDGE Events*, 97:1–2,24, 1992.
- [15] C.G. Fox, W.W. Chadwick, and R.W. Embley. Detection of changes in ridge-crest morphology using repeated multibeam sonar surveys. *J. of Geophys. Res.*, 97(B7):11149–11162, 1992.
- [16] J.S. Gombert and T.G. Masters. Waveform modeling using locked-mode synthetic and differential seismograms: application to determination of the structure of Mexico. *Geophys Journ. Roy. Astr. Soc.*, 94:193–218, 1988.
- [17] A.J. Harding, G.M. Kent, and J.A. Orcutt. A multichannel seismic investigation of upper crustal structure at 9°N on the East Pacific Rise: implications for crustal accretion. *J. of Geophys. Res.*, 98:13925–13944, 1993.
- [18] R.M. Haymon, D.J. Fornari, K.L. VonDamm, M. D. Lilly, et al. Volcanic eruption of the mid-ocean ridge along the East Pacific Rise at 9°45–52'N – direct submersible observations of seafloor phenomena associated with an eruption event in April, 1991. *Earth and Plan. Sci. Letters*, 119(1-2):85–101, 1993.

- [19] J.A. Hildebrand, J.M. Stevenson, P.T.C. Hammer, M.A. Zumberge, R.L. Parker, C.G. Fox, and P.J. Meis. A seafloor and sea surface gravity survey of Axial volcano. *J. of Geophys. Res.*, 95:4967–4987, 1990.
- [20] R. Houtz and J. Ewing. Upper crustal structure as a function of plate age. *J. of Geophys. Res.*, 81:2490–2498, 1976.
- [21] G.M. Kent, A.J. Harding, and J.A. Orcutt. Evidence for a smaller magma chamber beneath the East Pacific Rise at 9°30'N. *Nature*, 344:650–653, 1990.
- [22] G.M. Kent, A.J. Harding, and J.A. Orcutt. Distribution of magma beneath the East Pacific Rise between the Clipperton Transform and the 9°17'N deval from forward modeling of common depth point data. *J. of Geophys. Res.*, 98(B8):13945–13969, 1993.
- [23] L.J.B. Lacoste. Measurement of gravity at sea and in the air. *Rev. Geophys.*, 5:477–526, 1967.
- [24] K. MacDonald, J.C. Sempere, and P.J. Fox. East Pacific Rise from Siquieros to Orozco fracture zones: along-strike continuity of axial neo-volcanic zone and structure and evolution of overlapping spreading centers. *J. of Geophys. Res.*, 89:6049–6069, 1984.
- [25] J.A. Madsen, R.S. Detrick, J.C. Mutter, P. Buhl, and J.A. Orcutt. A two- and three-dimensional analysis of gravity anomalies associated with the East Pacific Rise at 9°N and 13°N. *J. of Geophys. Res.*, 95:4967–4987, 1990.
- [26] M.A. McDonald, S.C. Webb, J.A. Hildebrand, B.D. Cornuelle, and C.G. Fox. Seismic structure and anisotropy of the Juan de Fuca Ridge at 45°N. *J. of Geophys. Res.*, 99:4857–4873, 1994.
- [27] J.L. Morton, N.H. Sleep, W.R. Normark, and D.H. Tompkins. Structure of the southern Juan de Fuca Ridge from seismic reflection records. *J. of Geophys. Res.*, 92:11315–11326, 1987.
- [28] W.R. Normark, J.R. Delaney, G.S. Lichtman, J.L. Morton, J.L. Karsten, and H.P. Johnson. Geological and morphologic constraints on crustal-accretion models for the southern Juan de Fuca Ridge. *EOS, Trans. A. Geophys Un.*, 63:1146, 1982.

- [29] W.R. Normark, J.L. Morton, R.A. Koski, and D.A. Clague. Active hydrothermal vents and sulfide deposits on the southern Juan de Fuca Ridge. *Geology*, 11:158–163, 1983.
- [30] G.M. Purdy. New observations of the shallow seismic structure of young oceanic crust. *J. of Geophys. Res.*, 92:9351–9362, 1987.
- [31] G.M. Purdy, L.S. Kong, G.L. Christeson, and S.C. Solomon. Relationship between spreading rate and the seismic structure of mid-ocean ridges. *Nature*, 355:815–817, 1992.
- [32] K.M.M. Rohr, B. Milkereit, and C.J. Yorath. Assymmetric deep crustal structure across the Juan de Fuca Ridge. *Geology*, 16:158–163, 1988.
- [33] M.H. Salisbury and C.E. Keen. Listric faults imaged in oceanic crust. *Geology*, 21(2):117–120, 1993.
- [34] H. Schmeling. Numerical models on the influence of partial melt fraction on elastic, anelastic, and electric properties of rocks. Part I: elasticity and anelasticity. *Phys. Earth. Planet. Inter.*, 41:34–57, 1985.
- [35] J.M. Sinton and R.S. Detrick. Mid-ocean ridge magma chambers. *J. of Geophys. Res.*, 97(B1):197–216, 1992.
- [36] G.G. Sorrels and T.T. Goforth. Low frequency earth motion generated by slowly propagating, partially organized pressure fields. *Bull. Seismol. Soc. Am.*, 63:1583–1601, 1973.
- [37] P. Spudich and J.A. Orcutt. A new look at the seismic velocity structure of the oceanic crust. *Rev. Geophys.*, 18:627–645, 1980.
- [38] J.M. Stevenson, J.A. Hildebrand, M.A. Zumberge, and C.G. Fox. An ocean bottom gravity study of the southern Juan de Fuca Ridge. *J. of Geophys. Res.*, 99:4875–4888, 1994.
- [39] D.J. Thomson. Spectrum estimation techniques for characterization and development of WT4 waveguide I. *Bell Syst. Tech J.*, 56:1769–1813, 1977.
- [40] D.R. Toomey, G.M. Purdy, S.C. Solomon, and W.S.D. Wilcock. The three-dimensional seismic velocity structure of the East Pacific Rise near latitude 9°30'N. *Nature*, 347:639–645, 1990.

- [41] E.E. Vera, J.C. Mutter, P. Buhl, J.A. Orcutt, A.J. Harding, M.E. Kappus, R.S. Detrick, and T.M. Brocher. The structure of 0- to 0.2-m.y.-old oceanic crust at 9°N on the East Pacific Rise from expanded spread profiles. *J. of Geophys. Res.*, 95:15529–15556, 1990.
- [42] S.C. Webb, X. Zhang, and W. Crawford. Infragravity waves in the deep ocean. *J. of Geophys. Res.*, 96(C2):2723–2736, 1991.
- [43] D.J. White and R.M. Clowes. Shallow crustal structure beneath the Juan de Fuca Ridge from 2-d seismic refraction tomography. *Geophys. Journ. Int.*, 100:349–367, 1990.